
Politecnico di Torino

# POLITECNICO DI TORINO

MASTER'S DEGREE IN NUCLEAR AND ENERGY ENGINEERING

A.a. 2023/2024

# Advancements in wave energy conversion: a numerical analysis of the C4 CorPower WEC's dynamic response in various wave scenarios

**Advisor:**

**Prof. Eng. BRACCO Giovanni**

**Co-Advisors:**

**Prof. Eng. GRECO Marilena**

**Eng. BARDAZZI Andrea**

**Author:**

**DE MARINIS Francesco**

MARCH 2024

# Contents


**1 Introduction** **2**

1.1 Context and motivation . . . . . 2

1.2 Thesis objectives and structure . . . . . 5

**2 Wave Energy Converters (WECs)** **6**

2.1 Classification by location . . . . . 6

2.2 Operational principle . . . . . 7

2.3 Classification of oscillating WECs by wave direction . . . . . 9

2.4 Performance Evaluation of WECs . . . . . 12

2.5 Study Focus: C4 Point-Absorber by CorPower . . . . . 12

**3 WEC C4 by CorPower** **14**

**4 Theoretical background** **18**

4.1 Definition of motion . . . . . 18

4.2 Linear wave-induced loads and motions . . . . . 19

4.3 Response Amplitude Operator (RAO) . . . . . 24

4.4 Cummins' approach for time domain simulations . . . . . 24

4.5 Weakly nonlinear problem . . . . . 25

4.6 Viscous effects: correction in potential flow model . . . . . 26

**5 Numerical solution of the problem** **29**

5.1 Frequency domain solution . . . . . 29

5.2 Time domain solution . . . . . 30

**6 Verification and Validation of the software** **32**

6.1 Reference experimental data . . . . . 32

6.2 Input data for the frequency domain analysis . . . . . 33

6.3 Numerical convergence for the sphere: frequency domain results . . . . . 35

6.4 Influence of draft on added mass . . . . . 37

6.5 Free-decay time domain analysis and results . . . . . 38

**7 Analysis of WEC C4** **44**
7.1 Modeling of the hull of the WEC . . . . . 45
7.2 Numerical convergence for the WEC: frequency domain results . . . . . 45
7.3 Influence of draft on hydrostatic restoring, added mass and natural period 47
7.4 Time domain approach . . . . . 51
7.5 Results in free-decay . . . . . 52
7.6 Results in regular waves . . . . . 55
7.7 Results in irregular waves . . . . . 58

**8 Conclusions** **63**

**A Python scripts** **65**
A.0.1 Gmsh script for the meshed structure of the sphere . . . . . 65
A.0.2 Gmsh script for the meshed structure of the WEC hull . . . . . 66
A.0.3 Script for the interpolated curve of the natural period function of the draft . . . . . 67
A.0.4 Script for the interpolated curve of the added mass function of the draft . . . . . 68
A.0.5 Script for the interpolated curve of the diameter as function of the height of the structure . . . . . 70

# Acronyms and Abbreviations

- **WEC** - Wave Energy Converter
- **FFLOB** - Freely FLOating Body Analysis Software
- **TRL** - Technology Readiness Level
- **PTO** - Power Take-Off
- **RAO** - Response Amplitude Operator
- **BEM** - Boundary Element Method
- **CNR-INM** - Consiglio Nazionale delle Ricerche - Istituto iNgegneria del Mare
- **OWC** - Oscillating Water Column
- **STEPS** - Stated Policies Scenario
- **APS** - Announced Pledges Scenario
- **NZE** - Net Zero Emissions
- **PV** - PhotoVoltaics
- **IEA** - International Energy Agency
- **LCOE** - Levelized Cost of Energy
- **HDE** - Hydrodynamic Efficiency
- **KC** - Keulegan-Carpenter Number
- **DNV-RP-C205** - DNV Recommended Practices

# Abstract

This study examines the dynamic response of a selected wave energy converter (WEC) in long-crested waves ranging from linear to steep scenarios. First, an overview on the state-of-the-art for WECs is documented, also highlighting the fundamental role of renewable energy and carbon emission reduction in addressing environmental challenges. Various WECs technologies are discussed comparatively and, the innovative device, C4 CorPower WEC, proposed by CorPower is selected for an in-depth analysis. This is based on a point absorber solution, already at a high Technology Readiness Level (TRL).

The theoretical framework for the dynamic analysis is based primarily on linear potential-flow theory, but weakly-nonlinear hydrodynamic effects are also examined; moreover, viscous-flow effects are included through empirical formulas. The linear numerical approach includes: 1) a frequency-domain solution based on the zero-order boundary element method FFLOB, developed at CNR-INM, using the Green's function, and 2) a time-domain solution following the Cummin's approach, with Runge-Kutta time scheme, including nonlinear body dynamics and using a body-fixed reference frame. Weakly-nonlinear effects in the incident waves and in their induced loads can be included in the time domain formulation, stretching the applicability of the Cummin's approach. Preliminary numerical convergence studies are performed for a surface-piercing spherical buoy and validation analysis against available free-decay tests in heave at three different initial positions of the body, highlighting the importance of nonlinear effects. The sphere represents a relevant geometry as it shares similarities with the C4 CorPower WEC, which is an axisymmetric body with a substantial variation in the horizontal cross section. The selected device is described in detail, together with the simplified model of the different components and examined within a stepwise strategy. Within the frequency-domain analysis, it is first studied at the expected mean draft and the response amplitude operator (RAO) is evaluated for the relevant rigid degrees of freedom, then different values of the mean draft are assumed to quantify the effects on hydrostatic restoring, added mass and natural period in heave. Within the time domain analysis, free-decay tests in calm water and analyses in regular and irregular waves representing operational and severe sea environments, are examined. Both fully linear and weakly-nonlinear models are used. The selected wave conditions are taken from Agucadoura, in Portugal, a site of particular interest to CorPower, and for which, reference experimental and numerical data were made available by the company for comparison. Present study focuses on a detuned case where the device is not generating energy but is instead in a condition of storm protection. In this scenario, the device employs a high PTO (Power Take-Off) stiffness to ensure minimal heave movements, demonstrating the possibility to adapt in harsh sea environments. This approach explores paths for possible improvements of the system design, particularly in enhancing the operational flexibility of the WEC in facing extreme weather conditions.

# Chapter 1

# Introduction

## 1.1 Context and motivation

The quest for sustainable and environmentally friendly energy sources has raised importance in recent decades due to the pressing global issues of climate change and exhausting fossil fuel reserves [1]. In this context, renewable energy systems have emerged as an unique solution, offering the promise of reducing greenhouse gas emissions and mitigating the environmental impact of energy production. In fig. 1.1 are depicted three graphs illustrating the projected energy mix from 1990 to 2050 according to three different scenarios: Stated Policies Scenario (STEPS), Announced Pledges Scenario (APS), and Net Zero Emissions (NZE). Each graph displays the historical and projected energy contributions from various sources, including solar photovoltaics (PV), wind, hydro, nuclear, other renewables, unabated coal, unabated natural gas, other low-emissions, and other energy sources. The STEPS graph represents the energy outlook based on current policy settings, APS includes countries' specific policy intentions and targets, and NZE is aligned with achieving net-zero CO2 emissions by 2050. The shaded areas indicate the range of each energy source's contribution over time, reflecting the changes and growth in global energy production and consumption [2].

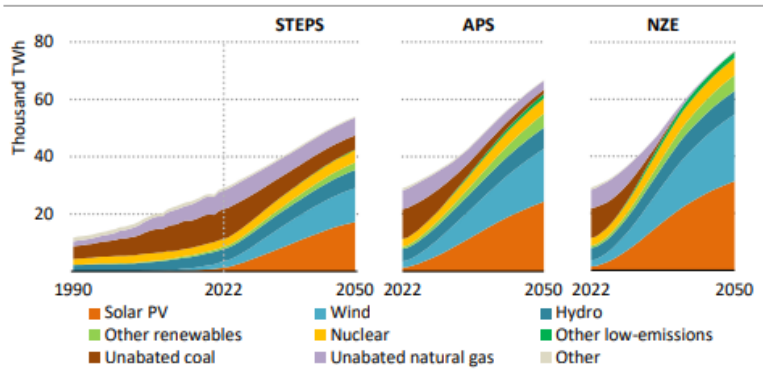


Figure 1.1: Global electricity generation by source and scenario, 1990-2050
Source: IEA, world energy outlook, 2023

Between the Renewable Energy Sources, ocean energy has garnered significant interest in recent years due to its distinctive attributes, which position it as an appealing addition to the renewable energy mix. Some of those benefits are represented in fig. 1.2 particularly emphasizing predictability, one of ocean energy's most interesting characteristics. Unlike other renewable sources that may be intermittent, ocean energy, offers a consistent and reliable energy flow. This predictability is crucial as it facilitates energy planning and grid management, ensuring a stable energy supply.

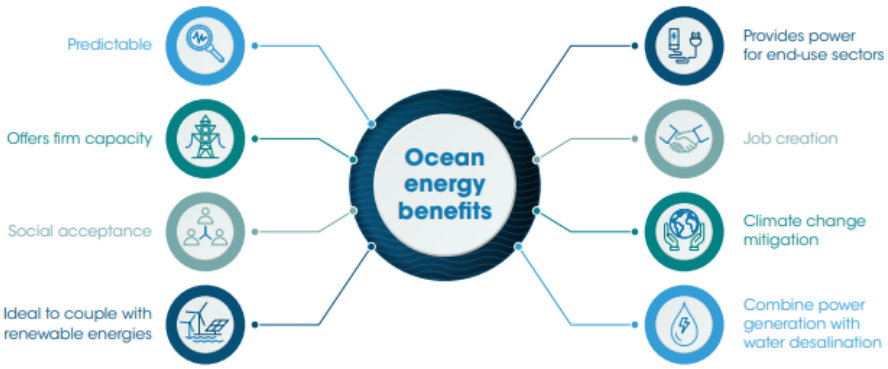


Figure 1.2: Benefits of ocean energy technologies
Source: Scaling up investments in ocean energy technologies, IRENA

Always referring to predictability , among the diverse array of ocean renewable energy sources, Wave Energy Converters (WECs) have gained particular attention as a promising technology that harnesses the energy present in ocean waves which potential is represented in fig. 1.3.

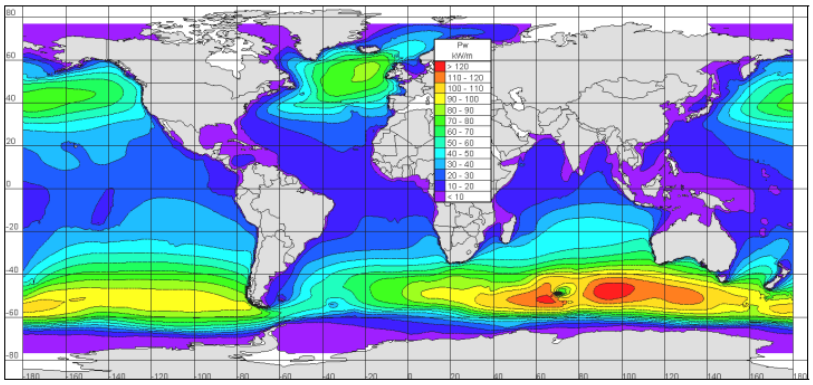


Figure 1.3: Global distribution of annual mean wave power
Source: Andrew Cornett, A Global Wave Energy Resource Assessment, 2008

This introduction will provide an overview of renewable energy systems, with a special focus on Wave Energy Converters, and highlight their significance in transitioning towards a more sustainable and cleaner energy future.

Renewable energy systems are those that draw power from sources that are naturally replenished over time, such as sunlight, wind, geothermal heat, and the movement of water. Their appeal lies in their ability to generate electricity without the release of greenhouse gases and other harmful pollutants, making them an essential component of global efforts to combat climate change. According to the International Energy Agency (IEA), renewable energy sources contributed to over 29% of global electricity generation in 2020, and this percentage is projected to grow exponentially in the coming years [3].

One of the most difficult challenges to face with the increasing RES is the development of appropriate infrastructure for energy storage and transmission.

Wave Energy Converters, a subset of marine renewable energy, focus on the vast and untapped potential of the world's oceans. These devices are designed to capture energy from the ocean waves and convert it into electricity [4]. The ocean's constant and inexhaustible wave energy makes WECs a promising technology with the ability to generate power continuously, reducing the reliance on intermittent energy sources like wind and solar. Their development is driven by their capacity to produce clean energy and their low carbon footprint.

This introduction serves as a foundation for exploring the domain of Wave Energy Converters, examining their different designs, operational principles, and the challenges they face. A comprehensive understanding of these systems is necessary for the transition towards sustainable energies, promoting a cleaner and more sustainable future for generations to come [1].

## 1.2 Thesis objectives and structure

The objective of this thesis is to analyze the dynamics of the CorPower Ocean's WEC C4 in an harsh sea environment.

To accomplish this objective, the thesis begins with a comprehensive review and classification of various WECs in Chapter 2, setting the stage for a deeper exploration into the field. Following this overview, the thesis delves into the characteristics and operational principles of the CorPower C4 WEC in Chapter 3, providing an understanding of its place in the realm of wave energy conversion. It is after presenting this foundational knowledge that the thesis then constructs the necessary theoretical background in Chapter 4, explaining the theory behind wave-body interaction dynamics, which is fundamental for the subsequent analysis.

Following the theoretical foundation, the thesis introduces the numerical strategies used for this study in Chapter 5. These solutions are essential for simulating the complex interactions between the WEC and its marine environment, allowing for a detailed examination of the WEC's response under various conditions.

An important step before the WEC's analysis is the validation phase, where the numerical results are compared with experimental data in Chapter 6. The examined case refers to free-decay tests of a sphere, which shares important features with the targeted WEC concept.

The thesis then specifically focuses on the CorPower C4 WEC in Chapter 7. By modeling the system and comparing surge free-decay simulation results to CorPower's own experimental findings, the study makes necessary adjustments to account for non-linear effects. This step is fundamental, as it enhances the model's accuracy by incorporating these critical factors into the base linear potential flow solution adopted as first step.

Finally, the thesis conducts simulations under both regular and irregular wave conditions. These tests are designed to simulate real-world marine environments, providing valuable insights into how the WEC operates under various wave scenarios.

# Chapter 2

# Wave Energy Converters (WECs)

WECs can be classified according to their operating principle, the direction of the incoming waves and the location of the Wave Energy Converter [5].

## 2.1 Classification by location

Wave energy converters are categorized according to their placement, which includes offshore, nearshore, and onshore configurations.

Offshore Locations: The higher wave energy levels found in deep waters make offshore devices more favorable for wave power generation. However, offshore devices face the challenges of severe climatic conditions, demanding deployment, and operational complexities.

Nearshore: Nearshore devices are typically deployed in shallower waters, often attached to the ocean floor.

Onshore: Onshore devices are situated along the shoreline, offering the advantage of easier maintenance and installation. They do not require deep-water moorings, and the risk of storm damage is minimal. However, the wave energy potential for onshore devices is generally less efficient.

The percentage of WECs referring to the location is represented in fig. 2.1

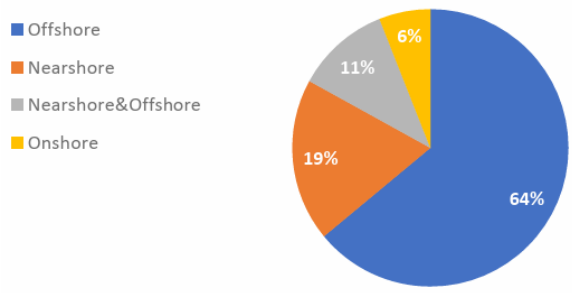


Figure 2.1: WECs based on location
Source: Dongsheng Qiao, Rizwan Haider, Jun Yan, Dezhi Ning and Binbin Li, Review of Wave Energy Converter and Design of Mooring Systemn, 2020

## 2.2 Operational principle

The operational principle of a wave energy converter (WEC) shows its interaction with and the absorption of energy from incoming waves. Here it is introduced a classification framework based on this operational principle and their share for this classification is represented in fig. 2.2.

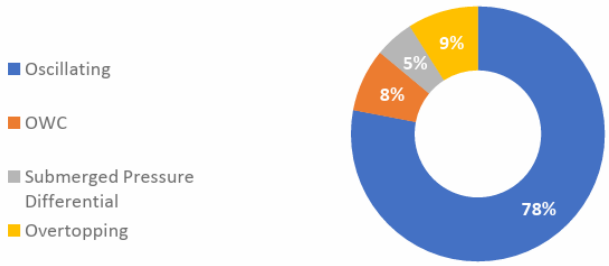


Figure 2.2: WECs based on operational principle
Source: Dongsheng Qiao, Rizwan Haider, Jun Yan, Dezhi Ning and Binbin Li, Review of Wave Energy Converter and Design of Mooring Systemn, 2020

One prominent type within this classification is the Oscillating Water Column (OWC) as in fig. 2.3. The OWC can either be a floating hollow or fixed device that utilizes the variations in water level induced by wave motion to compress and decompress air in its chamber. This process results in a pressure differential inside the chamber, compelling air to flow through a connected turbine that drives a generator. When located near the shoreline, OWCs serve the dual purpose of wave energy conversion and coastal protection, effectively functioning as breakwater structures. Several OWC devices have been

developed and implemented, each with unique characteristics and advantages. Notably, installations close to the shore offer inherent advantages.

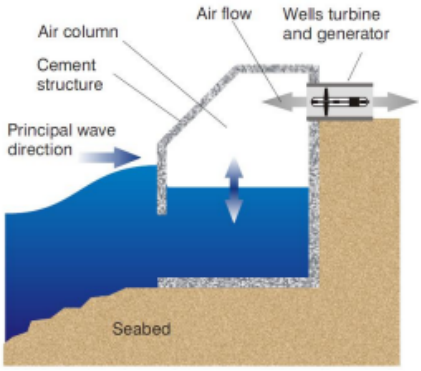


Figure 2.3: Oscillating Water Column device
Source: Daniela Dzhonova, Rumen Popov, Aleksandar Georgiev, Challenges of Marine Power in the Balkan Region, 2013

Oscillating Bodies is a broad category used to describe Wave Energy Converters (WECs) that harness power from wave-induced oscillations of submerged or floating structures, typically in the surge or heave motion as in fig. 2.4. Heaving-type devices are often designed as axisymmetric buoys positioned just below or at the water's surface, capturing energy from the vertical motion of the waves.

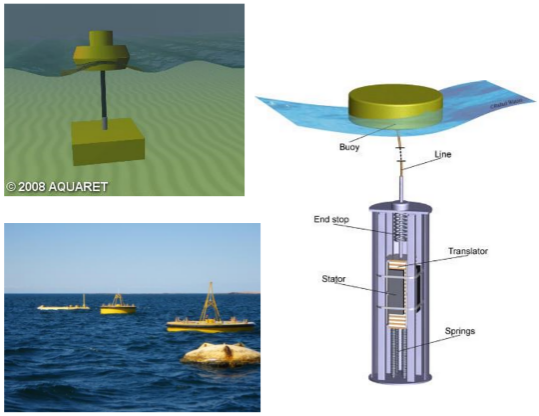


Figure 2.4: Oscillating bodies device
Source: E-nsight, L'energia del moto ondoso, 2020

Oscillating wave surge converters are commonly characterized by one end being anchored to a substructure or the seabed, while the opposite end remains free to move. Energy is harnessed from the relative motion of the device, which is driven by the horizontal movement of waves (surge), around the fixed anchored point.

Submerged Pressure Differential devices are securely anchored to the seabed, these devices are commonly known as submerged point absorbers and are located near the shore. They are constructed with one or more air-filled chambers, where the pressure changes due to incident waves, either troughs or crests. The dynamic pressure changes within these deformable chambers result in a continuous airflow within the device, which is subsequently converted into electricity by an air turbine.

An overtopping device, fig. 2.5, essentially operates as a wave energy converter that transforms the kinetic energy of ocean waves into potential energy. This potential energy is stored in a water reservoir, and its primary function is to ensure a steady supply to a conventional low-head hydraulic turbine or a series of such turbines.

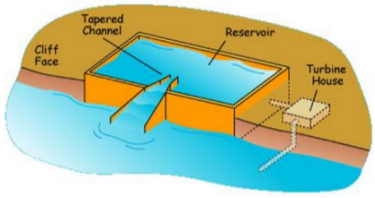


Figure 2.5: Overtopping device
Source: HKRENet, Wave Energy

## 2.3 Classification of oscillating WECs by wave direction

WECs can be categorized based on the direction of wave propagation fig. 2.6 fig. 2.7.

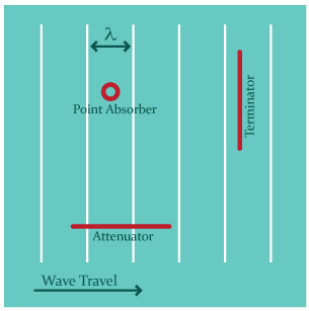


Figure 2.6: Wave direction classification
Source: Atargis Energy Corporation, CycWEC operational position

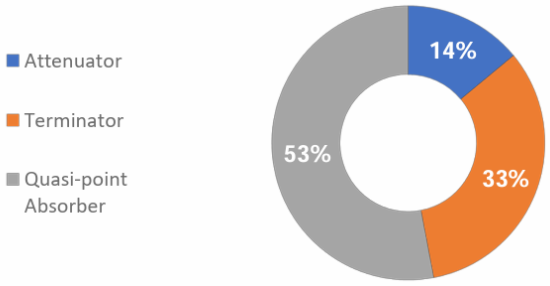


Figure 2.7: WECs based on orientation
Source: Dongsheng Qiao, Rizwan Haider, Jun Yan, Dezhi Ning and Binbin Li, Review of Wave Energy Converter and Design of Mooring Systemn, 2020

Attenuator: Typically, the attenuator is a flexible apparatus oriented parallel to the wave's direction of movement. It functions by capturing the energy generated from the relative motion of its sections, when waves pass through them as depicted in fig. 2.8. This type of device is designed to float on the water's surface, effectively harnessing wave energy in alignment with the wave's path.

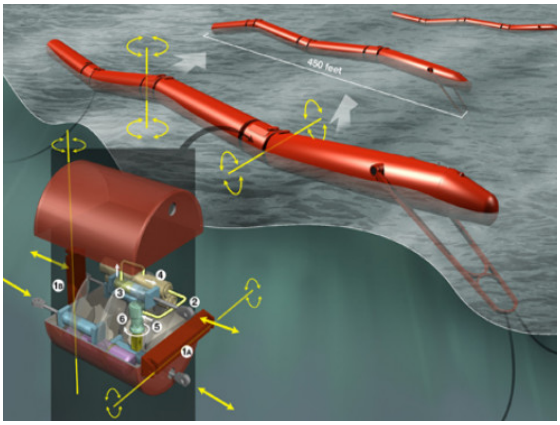

Figure 2.8: Attenuator WEC
Source: Md Jakir Hossain, Possibility and Methodology Investigation of Ocean Wave Power Generation, 2015

Terminator: In contrast, a Terminator WEC positions its principal axis parallel to the incoming wave crest, effectively 'terminating' the wave. These devices extend perpendicular to the wave's travel direction, capturing or reflecting the wave's energy as represented in fig. 2.9. While these devices are commonly located onshore or near the shore, floating versions have also been designed for offshore applications.

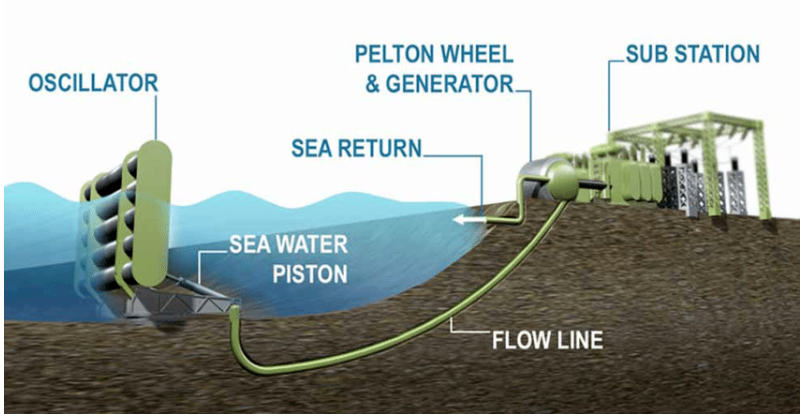


Figure 2.9: Terminator WEC
Source: Luca Collegiani, Analisi, modellazione e ottimizzazione del comportamento di un sistema di conversione per l'energia da moto ondoso, 2013-2014

Point Absorber: Point absorbers are characterized by their significantly smaller dimensions in comparison to a full wavelength. They possess the unique ability to generate power regardless of the direction of wave propagation. The buoy itself can oscillate along one degree of freedom or more. The buoy's motion, while undergoing damping, serves to extract energy, which is subsequently converted into electricity through a generator. These devices can be also characterized by two bodies in relative motion (float and heave plate) as represented in fig. 2.10.

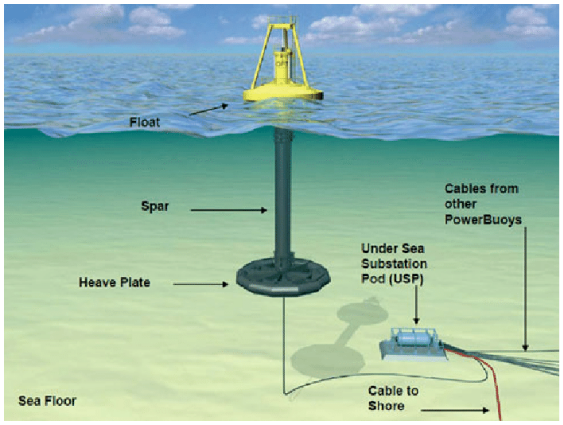


Figure 2.10: Point Absorber WEC
Source: Mirko Morini, Moto ondoso e maree, Sistemi di conversione dell'energia da fonti rinnovabili 2018-2019

## 2.4 Performance Evaluation of WECs

The development of WECs has garnered increased attention, with various types explored. To comprehensively assess their performance, the analysis of a WEC focuses on energy capture, technology cost, and reliability. Energy capture efficiency, an important factor for commercialization, is evaluated using the Hydrodynamic Efficiency (HDE) index. Multi-DOF WECs demonstrate the highest efficiency, followed by the terminator, point absorber, overtopping, and oscillating water column types, while attenuators perform the least efficiently. Also cost is a crucial consideration, cost analysis plays a crucial role in the development of wave energy capture technologies, and assessing the Levelized Cost of Energy (LCOE) is an essential step to understand their competitiveness in the energy market. Reliability depends on material and structural factors, with fewer parts exposed to seawater resulting in higher reliability, as seen in oscillating water column and overtopping converters. Conversely, point absorber, terminator, attenuator, and multi-DOF devices face potential reliability challenges, with multi-DOF converters being the most complex [6].

## 2.5 Study Focus: C4 Point-Absorber by CorPower

Notable examples within the category of point absorbers include the CorPower WEC in fig. 2.11, a floating WEC connected to a bottom-referenced pneumatic-mechanical drive that will be discussed in greater detail in the following sections.

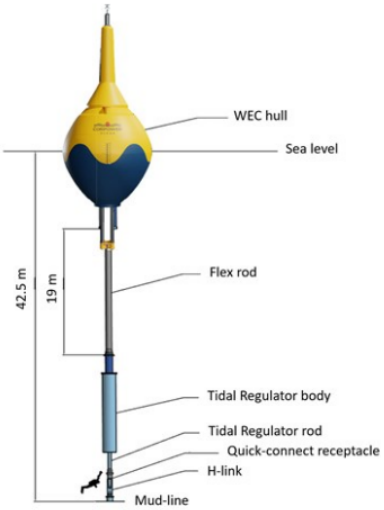


Figure 2.11: CorPower WEC
Source: https://www.autonational.de/neuigkeiten/corpower-ocean

In selecting to investigate a point-absorber technology such as the C4 by CorPower, several factors come into play. Firstly, the choice is justified by the versatility inherent in its design, particularly concerning wave directionality. The Aguçadoura site in Portugal, a site of particular interest for CorPower, presents diverse wave conditions, and a point-absorber like the C4 offers adaptability to varying wave angles, maximizing energy capture efficiency.

Moreover, the decision to focus on CorPower's concept is supported by its advanced stage of development and high Technology Readiness Level (TRL). By examining a technology at this stage, insights can be gained into its real-world applicability.

By studying the C4 point-absorber, this study aims to contribute to the understanding and advancement of this wave energy technology.

# Chapter 3

# WEC C4 by CorPower

CorPower C4, a point absorber Wave Energy Converter (WEC), represents a cutting-edge technology among the analyzed WECs. All the information presented in this chapter has been sourced from the official CorPower Ocean website [7]. The CorPower C4 has emerged as a remarkable innovation in the field of wave energy. Notably, it possesses several unique features that make it one of the most promising solutions in the wave energy sector.

The heart of this technology lies in a pre-tension system that anchors the heaving buoy. When wave swells push the buoy upwards, the stored hydraulic pressure within the system provides the necessary force to drive the buoy back downwards. This ensures that energy is harnessed in both upward and downward motions, resulting in a highly efficient and lightweight system.

CorPower Ocean, the company behind the CorPower C4, has positioned itself at the forefront of the wave energy revolution, in their technology the energy stored within the waves is seamlessly converted into electricity through the rise and fall, as well as the back-and-forth motion of the waves by Power Take Off (PTO) system that efficiently transforms mechanical energy into electricity.

Key innovations that define the CorPower C4 technology include Wavespring technology, a Cascade gearbox, a Pre-tension cylinder, a composite buoy design, UMACK anchors, and advanced control systems. Each of these elements contributes to enhancing energy production, improving efficiency, reducing costs, and extending the operational lifespan of the WEC. The Wavespring technology, for instance, introduces a negative spring function that leads to a threefold increase in energy production for a given buoy size, translating to increased revenue and cost-effectiveness.

Furthermore, CorPower C4 boasts advanced control technology, allowing the buoy to be tuned and detuned, adapting its response to varying sea conditions as shown in fig. 3.1.

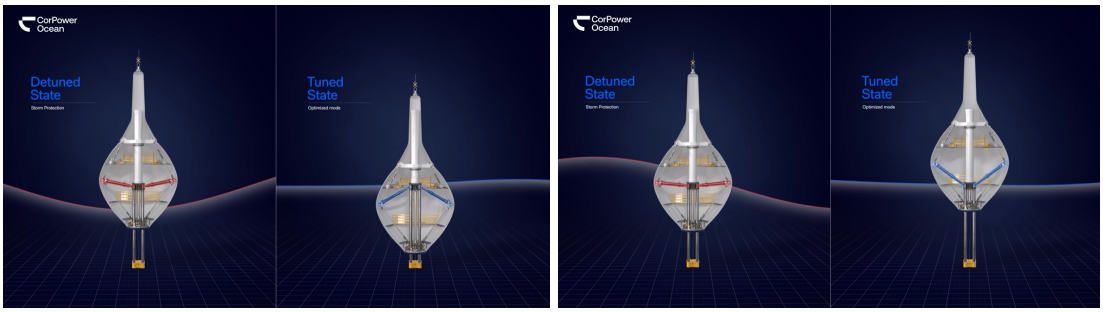


Figure 3.1: Tuned and detuned cases
Source: https://corpowerocean.com/

In stormy weather, the detuned state of the system makes it transparent to incoming waves, a safety feature akin to wind turbines that adjust their blades to prevent overloading. In normal sea conditions, the buoy is tuned to work in optimal timing with incoming waves, amplifying its motion and power capture. This fine-tuned control system allows for highly efficient wave energy capture, as it can amplify a 1-meter wave, for instance, into a buoy motion of 3 meters fig. 3.2.

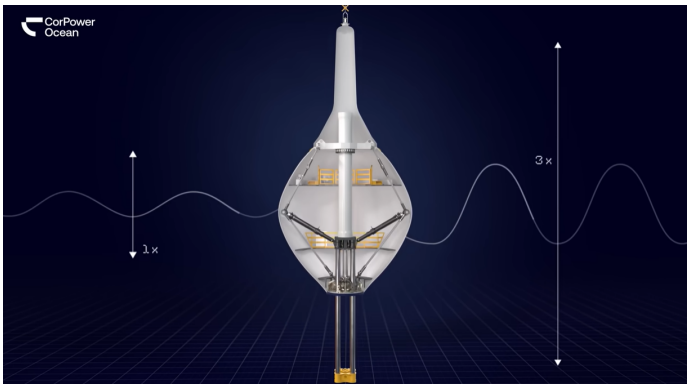


Figure 3.2: Amplification of the motion up to 3 times
Source: https://www.autonational.de/neuigkeiten/corpower-ocean

The CorPower C4 has key metrics that further underscore its capabilities, including a CorPack rating of 10-20 MW, an operational range (Hs) of 0.25-8 meters, a buoy diameter of 9 meters, spatial density of 15 MW/km$^2$, installation depth exceeding 40 meters, a height of 18 meters, a capacity factor ranging from 40% to 60%, a device rating of 300 kW, and a weight of 70 tonnes.

CorPower Ocean offers a comprehensive wave energy solution with its CorPack wave clusters. These clusters are made up of Wave Energy Converters, a mooring system, anchors, an electrical collection system, and a remote control and communication system. CorPacks are designed to be deployed side-by-side, forming larger wave farms with a total

capacity ranging from hundreds of megawatts to gigawatts. The electricity generated by each CorPack is efficiently exported through a collection hub, making it compatible with offshore wind energy installations.

The advantages of CorPower C4 extend beyond its technical capabilities. Its minimal visual impact is a notable feature, with devices protruding less than 10 meters above sea level. This attribute enhances its social acceptance as wave farms located only a few kilometers from the shore do not significantly disturb the coastal view.

Another key benefit of the CorPower C4 technology is its modular and efficient use of ocean space. With its spacial density, these wave farms can deliver three to five times more power from the same ocean space compared to a typical offshore wind farm. This remarkable high-density clustering approach empowers CorPower Ocean to provide a solution that efficiently utilizes the available ocean resources. In a manner similar to batteries constructed from many small cells packaged in modules, CorPower's wave clusters are comprised of numerous identical wave devices as shown in fig. 3.3. This modular approach facilitates efficient industrial deployment, fosters economies of scale, and encourages the involvement of local supply chains for construction, installation, and servicing. Consequently, this approach promotes high local content throughout the entire project life cycle.

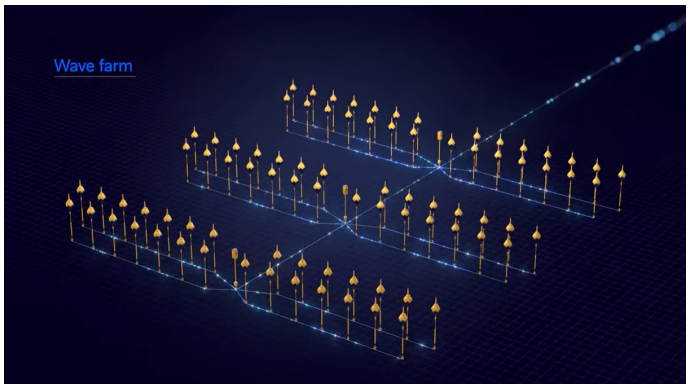


Figure 3.3: CorPower's wave clusters
Source: https://www.autonational.de/neuigkeiten/corpower-ocean

In summary, CorPower C4 is a groundbreaking point absorber Wave Energy Converter that leverages principles inspired by the human heart to efficiently harness the power of ocean waves. With advanced technology, innovative features, and a modular approach, it offers a sustainable and highly efficient solution for unlocking the vast energy potential of the oceans. This technology has the potential to revolutionize wave energy generation and contribute significantly to the transition to clean and renewable energy sources.

In order to advance the development of CorPower C4 technology, it becomes necessary to thoroughly comprehend the system's behavior within the challenging context of a harsh

sea environment. This thesis aims to contribute in this context through the utilization of a numerical simulation. Nevertheless, before focusing on the numerical analysis and the subsequent presentation of the achieved results, it is fundamental to furnish a scholarly introduction to the interactions of floating structure dynamics, the wave-body interaction phenomena, and the numerical solution strategy to perform this analysis.

# Chapter 4

# Theoretical background

The dynamic analysis of offshore structures forms a critical component of this study, focusing on assessing forces, motions, and accelerations of bodies in open sea conditions with uniform water depth. Through a comprehensive approach that extends beyond linear potential flow theory to include weakly non-linear hydrodynamic effects as well as the effects of viscous-flow through empirical formulas, the study aims to assess the following problem: analyzing the performance of a surface-piercing body under various marine conditions. This study delves into the dynamic analysis of the C4 wave energy converter in scenarios ranging from free decay to interactions with both regular and irregular waves, particularly under adverse sea states [8].

## 4.1 Definition of motion

To study the interaction problem between the wave and the floater, it is initially necessary to define a fixed Cartesian reference system, as shown in fig. 4.1. The origin of the earth fixed Cartesian reference system is located at on the mean free surface, which then represents the plane z=0. The x and y-axes lie in the plane of the free surface while the z-axis is oriented vertically upward. The six degrees of freedom of the body are subsequently represented and defined.

The translational motions along the axes are denoted as $\eta_1$, $\eta_2$, and $\eta_3$, while the rotational motions are denoted as $\eta_4$, $\eta_5$, and $\eta_6$. These variables can be used to represent the displacement of a generic point moving rigidly with the body as:

$$\vec{s} = \eta_1\mathbf{i} + \eta_2\mathbf{j} + \eta_3\mathbf{k} + \vec{\alpha} \times \vec{r} \tag{4.1}$$

With:

$$\vec{\alpha} = \eta_4\mathbf{i} + \eta_5\mathbf{j} + \eta_6\mathbf{k} \text{ (vector of angular motion)}$$

$$\vec{r} = x\mathbf{i} + y\mathbf{j} + z\mathbf{k} \text{ (position vector of the point of interest)}$$

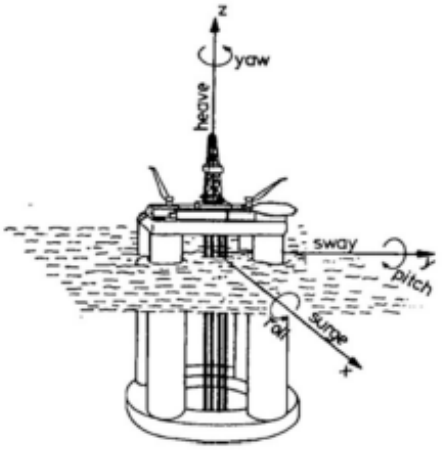


Figure 4.1: Definition of motions
Source: O.M. Faltinsen, Sea Loads on Ships and Offshore Structures

- **SURGE:** Translation along the X-axis
- **SWAY:** Translation along the Y-axis
- **HEAVE:** Translation along the Z-axis
- **ROLL:** Rotation around the X-axis
- **PITCH:** Rotation around the Y-axis
- **YAW:** Rotation around the Z-axis

## 4.2 Linear wave-induced loads and motions

In this study, linear potential flow theory is considered as an initial and valuable approach to analyze the behavior of the floater, specifically in terms of their motions and loads. This chapter's content is based on what is presented in the book Sea Loads On Ships and Offshore Structures [8].

The potential flow theory simplifies the mathematical treatment of fluid flow around objects under certain assumptions. These include:

1. **Inviscid Fluid:** The fluid is assumed to have no viscosity.
2. **Incompressible Fluid:** The fluid density is constant.
3. **Irrotational Flow:** The flow is irrotational, implying that the curl of the velocity field is zero, i.e., $\nabla \times \mathbf{V} = 0$. This allows representing the velocity field as the gradient of a scalar potential function $\phi$.

Given these assumptions, the velocity of the fluid at any point is derived from the potential function as:

$$\mathbf{V} = \nabla\phi = \mathbf{i}\frac{\partial\phi}{\partial x} + \mathbf{j}\frac{\partial\phi}{\partial y} + \mathbf{k}\frac{\partial\phi}{\partial z} \tag{4.2}$$

For an inviscid, incompressible, and irrotational flow, the Bernoulli equation can be expressed as:

$$p + \rho g z + \rho\frac{\partial\phi}{\partial t} + \frac{\rho}{2}\mathbf{V}\cdot\mathbf{V} = \mathrm{C} \tag{4.3}$$

The velocity magnitude $\mathbf{V}$ is related to the potential function $\phi$, allowing us to incorporate it into the Bernoulli equation.

So the problem can be linearized and studied by considering the velocity potential $\phi$ and solved using the system of the following equations referred to fig. 4.2:

$$\nabla^2\phi = 0 \quad \text{(Laplace's equation)} \tag{4.4}$$

$$\frac{\partial\phi}{\partial z} = 0 \text{ in } z = -h \quad \text{(horizontal seabed impermeability condition)} \tag{4.5}$$

$$\frac{\partial^2\phi}{\partial t^2} + g\frac{\partial\phi}{\partial z} = 0 \text{ in } z = 0 \quad \text{(combined linearized free surface condition)} \tag{4.6}$$

$$\frac{\partial\phi}{\partial n} = \vec{V}\cdot\vec{n} \text{ in } S_B \quad \text{(body impermeability condition)} \tag{4.7}$$

$$\lim_{r\to\infty} \nabla\phi = 0 \text{ at } r_\infty \quad \text{(far field condition with } r \text{ horizontal distance)} \tag{4.8}$$

Where $S_B$ is the mean wetted surface and $n$ is the normal vector into the body.

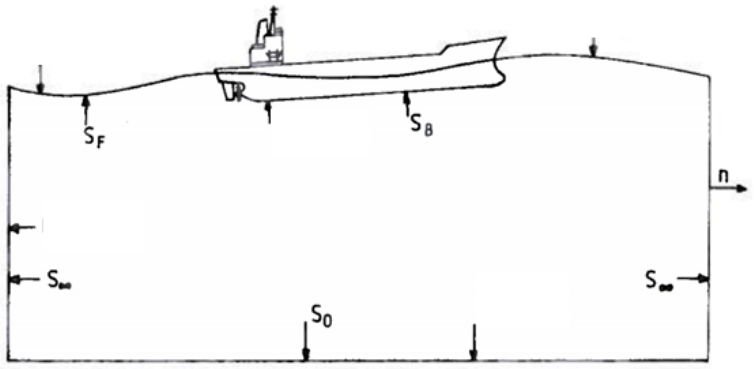


Figure 4.2: Control surface used to define the boundary conditions
Source: O.M. Faltinsen, Sea Loads on Ships and Offshore Structures

Considering the previously mentioned assumption of linearity, the problem can be decomposed into two distinct parts: one related to radiation and the other to diffraction. The overall outcome is the result of the superposition of these effects, as depicted in fig. 4.3.

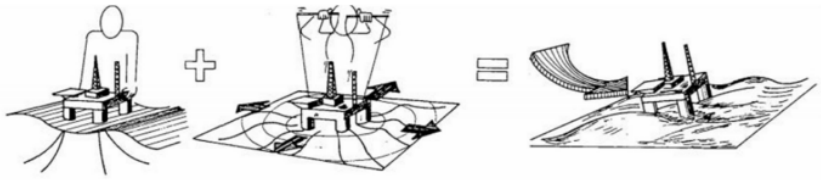

Figure 4.3: Decomposition of the problem
Source: O.M. Faltinsen, Sea Loads on Ships and Offshore Structures

In fluid dynamics and wave theory, the linear assumption simplifies the analysis of the body. A useful consequence of linear theory is that it is possible to obtain results in irregular waves by adding together results of regular waves (with constant amplitude and one frequency) with different amplitudes and wavelenghts, so it is sufficient to analyse the floater in incident regular sinusoidal waves of small wave steepness in a steady-state condition so that there are no transient effects and the induced loads and motion of the structure will oscillate with the excitation frequency, that allows to use the frequency domain analysis. Moreover, within linear theory, it is possible to separate the seakeeping problem into radiation and diffraction problems, which are associated to the two mechanisms involved in the wave-body interactions. The radiation part deals with the waves generated by the motion of the structure itself, while diffraction addresses the interaction of incident waves with the structure. The overall response of the structure is the combination of these two components. This approach enables a more tractable analysis of complex fluid-structure interactions.

In the diffraction problem, a stationary body is exposed to incident regular waves. The exciting loads (hydrodynamic loads) result from the summation of two contributions: one is an effect induced by the pressure field generated by the undisturbed waves as if the body were absent, leading to the Froude-Krylov loads. The other contribution envisions the body generating a flow that guarantees its impermeability as fixed structure, yielding the Diffraction or Scattering forces. Moving forward, the term 'forces' will denote generalized forces, encompassing both forces and moments acting on the body. Therefore, a force vector will comprise six components: the initial three represent forces, while the latter three represent moments.

In the radiation problem, on the other hand, one considers the body as forced to oscillate in its degrees of freedom within a wave-free environment. As the body moves, it generates forces acting upon it, thereby altering the fluid field. The forces derived from this scenario can be categorized into three components: Added Mass, Damping, and Restoring, each directly proportional to the acceleration, velocity, and displacement of the body.

Considering the linear problem, the potential can be decomposed into the sum of the radi-

ation potential and the diffraction potential. Consequently, $\phi(x,y,z,t) = \phi_R(x,y,z,t) + \phi_D(x,y,z,t)$. Assuming steady-state condition, within linear theory the loads and the response will oscillate as the input, so as the regular-incident waves; therefore the frequency domain analysis can be used. Using complex notation, the six-component vector of body motion can be written as $\eta = \eta_a e^{(i\omega t)}$. Moreover, the relationship $\phi(x,y,z,t) = \phi(x,y,z)e^{i\omega t}$ can be defined, indicating that the time and space dependence of the velocity potential can be separated in steady-state conditions. The diffraction potential can, in turn, be considered as the sum of the wave potential without the body and the scattering potential: $\phi_D = \phi_W + \phi_7$. Splitting the space and time dependence, the first one can be rewritten as $\frac{ga}{\omega} e^{k(z-i(x\cos\beta + y\sin\beta))}$, where $a$ is the wave amplitude, $\beta$ is the angle of incidence, $\omega$ is the circular frequency, and $k = \frac{2\pi}{\lambda}$. The radiation potential is given by $\sum_{j=1}^{6}(\dot{\eta}_j \phi_j)$, where $\phi_j$ is the potential associated with unitary body velocity in the $j$ direction.

The boundary conditions to solve this problem are as follows:

$$\nabla^2\phi = 0 \quad \text{(Laplace's equation)} \tag{4.9}$$

$$\frac{\partial \phi_j}{\partial z} = 0 \text{ in } z = -h \quad \text{(impermeability condition on the seabed)} \tag{4.10}$$

$$\text{-}\omega^2\phi_j + g\frac{\partial \phi_j}{\partial z} = 0 \;\; \text{with } \jmath = 1,\ldots,7 \quad \text{(unified free surface condition)} \tag{4.11}$$

$$\frac{\partial \phi_j}{\partial n} = n_j \text{ with } \jmath = 1,\ldots,6 \quad \text{(body boundary condition)} \tag{4.12}$$

$$\frac{\partial \phi_j}{\partial n} = -\frac{\partial \phi_w}{\partial n} \text{ with } j = 7 \quad \text{(body boundary condition)} \tag{4.13}$$

$$\lim_{r\to\infty} \sqrt{r}\left(\frac{\partial \phi_j}{\partial r} - ik\phi_j\right) = 0 \text{ with } \jmath = 1,\ldots,7 \quad \text{(radiation and far-field condition)} \tag{4.14}$$

The potential obtained in this way is complex, characterized by both magnitude and phase, representing either lead or lag with respect to the incident wave. The numerical solution of the presented problem will be explained later.

For the radiation problem to obtain the dynamic pressure, it is possible to use equation 4.3 to express the radiation force as:

$$\mathbf{F}_{rad,k} = -\rho \int_{S_B} \frac{\partial \phi_R}{\partial t} \vec{n}_k \, dS_B \quad \text{with } k = 1,\ldots,6 \tag{4.15}$$

By integrating the linear dynamic pressure, multiplied by the normal vector, over the surface for the desired force component, the expression can be reformulated as:

$$\mathbf{F}_{rad,k} = -\sum_{j=1}^{6}[A_{kj}\frac{\partial^2\eta_j}{\partial t^2} + B_{kj}\frac{\partial\eta_j}{\partial t}] \tag{4.16}$$

Where $A_{j,k}$ is the added mass coefficient, and $B_{j,k}$ is the damping coefficient, calculated as:

$$A_{j,k} = \rho Re\left[\int_{S_B}\phi_j\mathbf{n_k}dS_B\right] \tag{4.17}$$

$$B_{j,k} = -\rho\omega Im\left[\int_{S_B}\phi_j\mathbf{n_k}dS_B\right] \tag{4.18}$$

Integrating the hydrostatic pressure on the instantaneous wetted body surface up to $z = 0$ and subtracting the mean buoyancy we get the hydrostatic restoring forces due to the body motions. They are formally as $F_{hyd,k} = -\sum_j C_{kj}\eta_j$

For an unmoored structure with vertical symmetry, such as in the case of a buoy, the only non-zero $C_{j,k}$ elements are:

$$C_{33} = \rho g A_W \tag{4.19}$$

$$C_{35} = C_{53} = -\rho g\int\int_{A_W} x dS \tag{4.20}$$

$$C_{44} = \rho g V\overline{GM_T} \tag{4.21}$$

$$C_{44} = \rho g V\overline{GM_L} \tag{4.22}$$

Where $A_W$ is the waterplane area, the surface area of the body's hull at the waterline level, and for a moored structure additional restoring forces must be added.

From the diffraction problem is possible to obtain the exciting force dependent from the wave amplitude a:

$$F_{ex,K} = -i\omega\rho\int_{S_B}\frac{\partial\phi_7}{\partial t}n_k dS_B - \rho\int_{S_B}\frac{\partial\phi_w}{\partial t}n_k dS_B = Re\left\{aX_k e^{(i\omega t)}\right\} \text{ with k = 1,...,6} \tag{4.23}$$

Where the two contributions of the k-component of the excitation-force are, respectively, the Scattering and the Froude-Krylov forces. They are obtained integrating the corresponding linear dynamic pressure (multiplied by $n_k$) along the mean wetted surface of the body.

## 4.3 Response Amplitude Operator (RAO)

Within a linearized model in steady state conditions, having defined the terms for radiation and diffraction forces, it is possible to calculate the hydrodynamic forces based on the second law of Newton applied to the problem of floaters:

$$\mathbf{F} = \mathbf{M}\ddot{\boldsymbol{\eta}} \tag{4.24}$$

where $\mathbf{F} = \mathbf{F}_{rad,k} + \mathbf{F}_{hyd,k} + \mathbf{F}_{ex} + \boldsymbol{F_{PB}}$ where $\boldsymbol{F_{PB}}$ gives the generalized force contribution from weight and buoyancy.

Using complex notation, we can obtain:

$$[-\omega^2(\mathbf{M} + \mathbf{A}) + iw\mathbf{B} + \mathbf{C}]\eta_{\mathbf{a}}e^{i\omega t} = a\mathbf{X}e^{i\omega t} \tag{4.25}$$

From which we can derive:

$$\frac{\eta_{\mathbf{a}}}{a} = [-\omega^2(\mathbf{M} + \mathbf{A}) + i\omega\mathbf{B} + \mathbf{C}]^{-1}\mathbf{X} \tag{4.26}$$

that represents the Response Amplitude Operator (RAO), providing the complex transfer function of the body motions in terms of amplitude and phase. The transfer function of the amplitude gives the amplitude per unite incident-wave amplitude and the phase gives the deterministic phase relative to the incident-wave.

## 4.4 Cummins' approach for time domain simulations

The Cummins' approach provides a powerful framework for simulating the response of the floater in the time domain [9], allowing for the analysis of transient scenarios and scenarios involving multiple frequencies. This methodology bridges the gap between frequency-domain analyses and the need for time-domain solutions, particularly useful in complex sea states or when considering the interaction of waves with varying characteristics.

Cummins' approach is based on the convolution integral that relates the motion of a floating body to the applied wave forces over time. The equation can be represented as:

$$(\mathbf{M} + \mathbf{A}(\infty))\ddot{\eta}(t) + \int_0^t \mathbf{K}(t-\tau)\dot{\eta}(\tau)d\tau + \mathbf{C}\eta(t) = \mathbf{F}(t) \tag{4.27}$$

where:

- $\mathbf{M}$ is the mass matrix of the floating structure.
- $\mathbf{A}(\infty)$ is the added mass at infinite frequency.
- $\mathbf{K}(t-\tau)$ represents the impulse response function, derived from the frequency-

dependent damping. It describes how the damping changes over time, incorporating the effects of radiation damping that depend on past motions.

- $\mathbf{C}$ is the hydrostatic stiffness matrix.
- $\eta(t)$ is the vector of body motions (heave, sway, roll, etc.).
- $\mathbf{F}(t)$ is the excitation force vector as a function of time.

## 4.5 Weakly nonlinear problem

Nonlinear effects play a critical role in accurately predicting the response of floating structures to wave interactions. Traditional linear models, while foundational, are sometimes not enough to study the complex dynamics arising from nonlinear interactions. This limitation is particularly evident when, for example, resonance for certain degrees of freedom occurs at natural frequency outside the incident-wave frequency range so that in steady-state condition it cannot be excited by linear effects, but it could by second or higher-order effects. To address these complexities, the perturbation approach extends the analysis to encompass second- and higher-order effects. Focusing on second-order effects, a systematic approach necessitates the incorporation of second-order models for both incident wave dynamics and wave-body interactions.

Weakly non-linear models aim to simplify the fully non-linear formulation. In these models, a perturbation expansion is performed based on the wave steepness ($ka$), where $k$ represents the wave number and $a$ is the wave amplitude. The boundary conditions are approximated using their Taylor expansion. The perturbation method is applied to solve for the lowest degree of steepness, and these solutions are used as input for higher-order terms. Typically, a second-order approximation is used, where the (linear) solution in $ka$ is employed to solve for $(ka)^2$. Codes utilizing this second-order approximation are more effective in describing diffraction and excitation problems [10].

The weak-scatterer approximation is a simplification that can be used, which assumes that the waves and the body motions can be large, so second order effects are included, but radiation and scattering effects are limited and can be modelled with a correction of their linear prediction.

In this study three different effects are analysed:

1. Radiation scattering correction: the model assumes an impermeable body, with its movement affecting the surrounding wave field. The normal velocity component at the hull is derived from the relative motion between the floater and the waves, averaged across the wetted surface. This approach integrates the radiation and scattering phenomena, which are then processed through a convolution integral that is informed by specific hydrodynamic coefficients [11].

2. Nonlinear hydrostatic: the hydrostatic restoring coefficient $\mathbf{C}$ is no more calculated considering a mean wetted surface configuration but the instantaneous wetted surface is calculated every time step and so it becomes function of the body motion $\mathbf{C}(\eta)$

3. Viscous effects: viscous effects are taken into account via empirical formulas as it will be analysed in the following section.

## 4.6 Viscous effects: correction in potential flow model

Linear potential flow models simplify their analysis by ignoring the effects of viscosity, assuming the fluid is inviscid. However, if the body has elements with cross-section small relative to the incident-wave length and height then flow separation mechanisms are expected and viscous-flow effects should be included in the loads and it is suggested that the significance of viscous effects should be acknowledged by incorporating them externally. Viscous losses are contingent on the device's velocity relative to the fluid, with these losses exhibiting linear and quadratic dependence on velocity. Morison's equation is commonly used to model the viscous forces on a cylindrical structure. According to Morison's equation the horizontal force on a fixed strip of length dz can be written as:

$$\boldsymbol{dF} = \rho\frac{\pi D^2}{4}C_m\boldsymbol{a_1}dz + \frac{\rho}{2}C_D D|\boldsymbol{u}|\boldsymbol{u}dz \tag{4.28}$$

Where $\rho$ is the mass density of the water, $D$ is the diameter of the cylinder, $u$ and $a_1$ are the horizontal undisturbed fluid velocity and acceleration. The mass and and drag coefficient have to be empirically determined since they are dependent on the KC and Reynolds numbers.

Considering the modified Morison's equation for a moving circular cylinder and focusing on the inertial term:

$$\boldsymbol{dF} = \underbrace{\rho\frac{\pi D^2}{4}C_m\boldsymbol{a_1}dz}_{Mass} + \underbrace{\frac{\rho}{2}C_D D(\boldsymbol{u}-\dot{\boldsymbol{s}})|\boldsymbol{u}-\dot{\boldsymbol{s}}|dz}_{Drag} - \underbrace{\rho(C_m-1)\frac{\pi D^2}{4}\ddot{\boldsymbol{s}}dz}_{Added\ mass} \tag{4.29}$$

Where $C_m - 1 = C_a$ represents the added mass coefficient and $\boldsymbol{u}$ and $\boldsymbol{a_1}$ represent respectively the velocity and the acceleration of the flow. The acceleration of the body can be written considering eq. (4.1) as follows:

$$\ddot{\boldsymbol{s}} = \ddot{\boldsymbol{\xi}}_{\boldsymbol{1}} + \begin{bmatrix} 0 & z & 0 \\ -z & 0 & 0 \\ 0 & 0 & 0 \end{bmatrix} \ddot{\boldsymbol{\xi}}_{\boldsymbol{2}}$$

where z is the coordinate of the mooring, $\ddot{\boldsymbol{\xi}}_{\boldsymbol{1}}$ represents the vector $(\ddot{\eta}_1, \ddot{\eta}_2, \ddot{\eta}_3)$ and $\ddot{\boldsymbol{\xi}}_{\boldsymbol{2}}$

represents the vector $(\ddot{\eta}_4, \ddot{\eta}_5, \ddot{\eta}_6)$ and so the first 3 components of the added mass can be obtained integrating the elementary 3D added-mass force

$$\boldsymbol{dF} = \rho A C_A I \ddot{\boldsymbol{\xi}}_{\mathbf{1}} dz + \rho A C_A \begin{bmatrix} 0 & z & 0 \\ -z & 0 & 0 \\ 0 & 0 & 0 \end{bmatrix} \ddot{\boldsymbol{\xi}}_{\mathbf{2}} dz$$

and the second 3 components can be obtained integrating the torque of the elementary 3D force

$$\boldsymbol{dM} = \boldsymbol{r} \times \boldsymbol{dF}$$

and more explicitly

$$\boldsymbol{dM} = \rho A C_A \begin{bmatrix} 0 & -z & 0 \\ z & 0 & 0 \\ 0 & 0 & 0 \end{bmatrix} \ddot{\boldsymbol{\xi}}_{\mathbf{1}} dz + \rho A C_A \begin{bmatrix} z^2 & 0 & 0 \\ 0 & z^2 & 0 \\ 0 & 0 & 0 \end{bmatrix} \ddot{\boldsymbol{\xi}}_{\mathbf{2}} dz$$

The integration should be performed from the seabed to the coordinate of the fairlead, giving

$$\boldsymbol{M} = \rho A \frac{C_A}{2} \begin{bmatrix} 0 & -z^2 & 0 \\ z^2 & 0 & 0 \\ 0 & 0 & 0 \end{bmatrix} \ddot{\boldsymbol{\xi}}_{\mathbf{1}} + \rho A \frac{C_A}{3} \begin{bmatrix} z^3 & 0 & 0 \\ 0 & z^3 & 0 \\ 0 & 0 & 0 \end{bmatrix} \ddot{\boldsymbol{\xi}}_{\mathbf{2}} \Bigg|_{z=seabed}^{z=fairlead}$$

In Morison's equation the drag coefficient, $C_D$, is dependent on both the Reynolds number (Rn), as calculated by $\frac{U_m D}{\nu}$, and the Keulegan-Carpenter number, $KC$, defined by $KC = \frac{U_m T}{D}$. Here $U_m$ represents the relative velocity between the body and the flow, $\nu$ is the kinematic viscosity, $T$ is the characteristic period of oscillation, $D$ is the cylinder's diameter. Here, the DNV Recommendation Practice are followed [12], so:

1. For Rn $> 10^5$:

$$\psi(KC) = \begin{cases} C_\pi + 0.10(KC - 12), & \text{for } 2 \leq KC < 12 \\ C_\pi - 1.00, & \text{for } 0.75 \leq KC < 2 \\ C_\pi - 1.00 - 2.00(KC - 0.75), & \text{for } KC \leq 0.75 \end{cases} \tag{4.30}$$

   where:

$$C_\pi = -1.50 - 0.024(12/C_{DS} - 10)$$

   For intermediate roughness, the values are found by linear interpolation between the curves for smooth and rough cylinder corresponding to $C_{DS} = 0.65$ and $C_{DS} = 1.05$.

2. For Rn $< 10^5$:

$$C_D = \begin{cases} C_{D1} = \dfrac{3\pi^3}{2KC}\left((\pi\beta)^{-1/2} + (\pi\beta)^{-1} - \dfrac{1}{4}(\pi\beta)^{-3/2}\right), & \text{for } KC < KC_0 \\ C_{D2} = 0.2KC, & \text{for } KC_0 < KC < 10 \\ C_{D3} = 1.2[1 + 0.58e^{-0.064KC}]^2, & \text{for } KC > 10 \end{cases} \tag{4.31}$$

Assuming a value of the $KC_0$ equal to 1.8 and where $\beta = \frac{D^2}{\nu T}$ [13].

According to the DNV recommended practices, as illustrated in fig. 4.4 the coefficient's values for a cylinder depend on surface roughness and the Keulegan-Carpenter number[12].

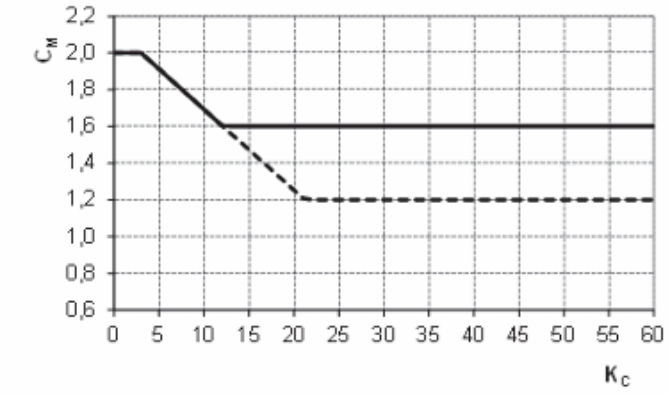


Figure 4.4: Cm as function of KC number for smooth (solid line) and rough (dotted line) cylinders

Source: Environmental conditions and environmental loads. DNV-RP-C205, 2014

# Chapter 5

# Numerical solution of the problem

The dynamic analysis framework relies on the linear potential-flow theory, integrating weakly-nonlinear hydrodynamic effects and incorporating viscous-flow effects via empirical formulas. The linear analysis consists of a frequency-domain solution using a zero-order boundary element method, performed through FFLOB, a software developed by CNR-INM, using Green's function, together with a time-domain solution following to Cummin's methodology with a Runge-Kutta time-stepping scheme. This approach accounts for non-linear dynamics of the body within a body-fixed reference frame, and permits inclusion of weakly-nonlinear effects from incident waves and their resulting loads in the time domain, so stretching the applicability of Cummin's approach [9].

Thus an acceptable model can be obtained through the fundamental assumptions of fluids being incompressible, inviscid, and irrotational, with negligible surface-tension effects, for which the potential flow theory is valid. As already introduced there are two principal methodologies: frequency-domain analysis and time-domain analysis, which provides a direct approach for simulations over time.

## 5.1 Frequency domain solution

In the frequency domain, the numerical approach requires evaluating the solution across a selected set of frequencies. For each frequency, the system of equations associated with the complex velocity potential $\phi_j$, is solved numerically through a direct boundary integral method using the Green's function. This involves inverting a new coefficient matrix for each frequency, due to the frequency dependency introduced by the Green's function.

For the numerical solution, a zeroth-order Boundary Element Method (BEM) is utilized. The submerged part of the body is discretized into $N$ flat panels, with each panel maintaining a constant potential value, $\phi_j$ , where $j = 1 \dots 7$. The discretization facilitates the approximation of the body boundary condition by enforcing a uniform velocity potential across each element. Consequently, the problem is represented as a system of linear equations for the centroids of the $N$ panels.

This leads to seven algebraic equation systems, each with N unknowns. They share the same (full) matrix, which make more efficient their numerical solution. As the problems depend on the involved frequency, one needs to solve seven problems for each frequency, but the zero and infinite frequency cases represent special scenarios considering that they correspond to zero vertical velocity and zero velocity potential on the free-surface, respectively. Once $\phi_j$ is found, the added-mass and wave-radiation damping coefficients, as well as the excitation forces can be estimated and be used in eq. (4.26) to estimate the RAOs.

To sum up, the frequency-domain analysis tool, FFLOB, inputs a discretized geometry of the submerged part of the body along with a file containing the selected frequencies and outputs added mass and damping coefficients, as well as the real and imaginary parts of the excitation forces.

## 5.2 Time domain solution

This analysis adopts a time-domain approach to address the problem, within the context of mean free-surface and body setups and using the frequency domain results for the time domain. This is achieved through the reconstruction of the solution over time by applying the Fourier transform operator to the impulse response. The current approach is noted for its effectiveness in solving these problems, though it has limited applicability. To stretch the applicability of the linear solution it is possible to account for nonlinear hydrostatic effects by calculating the hydrostatic pressure on the instantaneous wetted surface defined by the body motions and the incident waves, similarly can be done for the Froude-Krylov forces, for the integration of the linear dynamic pressure of the incident waves and including also quadratic-velocity term in the pressure. Finally, one can also include viscous-flow effects through the Morison's equation. These forces are directly integrated on the body motion, enhancing the accuracy of computing the instantaneous body-boundary condition on the actual wetted hull surface in the presence of incident waves.

The refinement of this approach includes the consideration of the Cummins equation within the solution algorithm, where $M$, representing the body mass properties, is predetermined. The infinite-frequency added mass $A_\infty$ and damping $B$ coefficients are determined using FFLOB software, allowing for the evaluation of forces at any given time instant. With the forces known at any time, the equation of motion can be integrated over time through either a third or fourth-order Runge-Kutta scheme. This method, known for its simplicity and robustness, involves numerically integrating ordinary differential equations by using a trial step at the midpoint with an explicit/implicit iterative method [14]. The third-order Runge-Kutta formula, which will be specified, is fundamental to this approach's efficacy in enhancing the computational precision of dynamic interactions with incident waves.

The flow diagram of the complete frequency and time domain solver is given in 5.1.

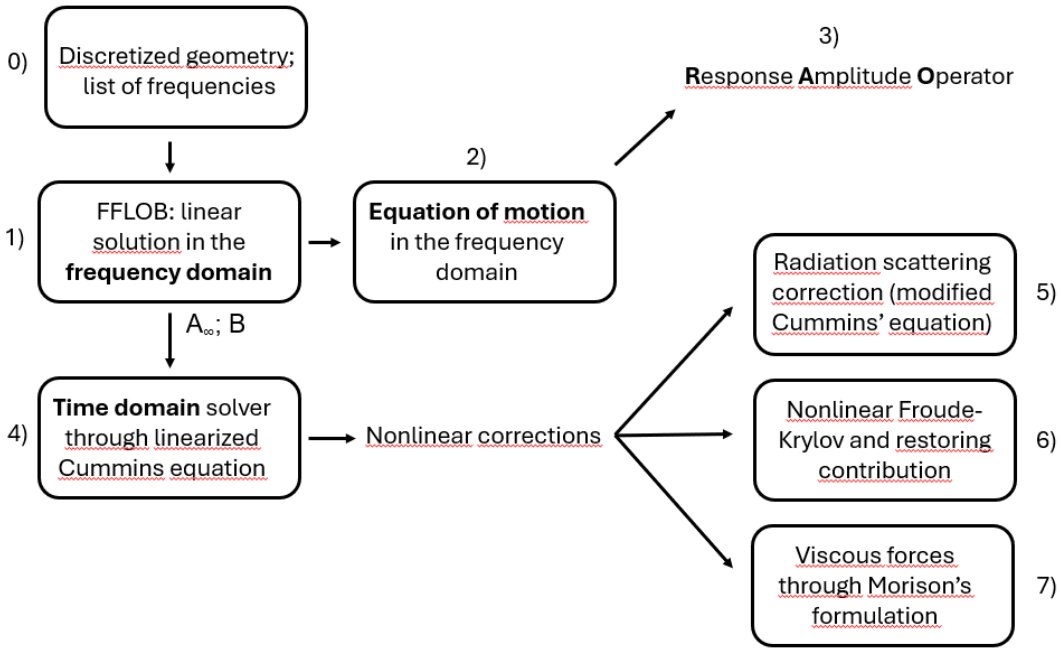


Figure 5.1: Flow diagram of the complete frequency and time domain solver

This formulation enables the accurate integration of the equation of motion over time, employing a balanced approach that considers both computational efficiency and the accuracy necessary for assessing dynamic pressures and forces on the wetted surface of the body.

In the upcoming chapter, the initial step involves a validation process of the software that implements the numerical solution before delving into the CorPower C4 hydrodynamic analysis.

# Chapter 6

# Verification and Validation of the software

The validation step is undertaken to ensure the accurate and reliable functioning of the underlying software. It serves as a necessary check to confirm that the computational tool is appropriately capturing and representing the physical phenomena associated with the hydrodynamic behavior of the CorPower C4 system.

By subjecting the software to validation, the aim is to establish confidence in the numerical results and their alignment with real-world observations. This not only safeguards against potential errors but also enhances the credibility of subsequent analyses and findings. The validation process typically involves comparing the software's predictions with more general solutions, as for example experimental data, or validated numerical results from similar cases.

Only after successfully illustrating this validation step will the work proceed with some verification steps of convergence studies and with the in-depth analysis of the CorPower C4 hydrodynamics.

The plots in this chapter, providing dimensional quantities, give their dimensions in the SI units.

## 6.1 Reference experimental data

The experiments taken as reference [15] for the validation step were conducted using an unmoored sphere subjected to heave decay tests in a controlled wave basin. The primary parameters defining the experimental setup are summarized in table 6.1.

| Parameter | Value |
|---|---|
| Sphere Diameter | 0.3 [m] |
| Sphere Mass | 7.056 [kg] |
| Material Density | 998.2 [kg/m$^3$] |
| Water Depth | 0.9 [m] |
| CoG | $(0, 0, -0.0348)$ [m] |
| $I_{xx}$ | $98251E3$ [gmm$^2$] |
| $I_{yy}$ | $98254E3$ [gmm$^2$] |
| $I_{zz}$ | $73052E3$ [gmm$^2$] |
| $I_{xz}$ | $0E3$ [gmm$^2$] |
| $I_{xy}$, $I_{xy}$ | $10E3$ [gmm$^2$] |

Table 6.1: Summary of Experimental Parameters

Heave decay tests were performed to capture the natural oscillation and damping characteristics of the spherical model. The test outcomes, specifically the decay rates and natural frequencies, are critical for validating the simulation results. Initial condition test data are presented in table 6.2.

| Initial Displacement | Value |
|---|---|
| $H_0$ [m] | $0.1D$ |
| $H_0$ [m] | $0.3D$ |
| $H_0$ [m] | $0.5D$ |

Table 6.2: Initial condition for the Heave Decay Test

## 6.2 Input data for the frequency domain analysis

As already explained, FFLOB uses as input data a discretized geometry of the body and a list of frequencies for which the problem is to be solved. This section explains how these are constructed.

Starting with the mesh, it is created using Gmsh [16], an open-source 3D finite element mesh generator with a built-in CAD engine and post-processor. The two types of meshes that have been created differ in the type of finite elements used: in the case of a structured mesh, they are all regular and ordered, unlike the case of the unstructured mesh. The structured mesh was created by drawing a curve equivalent to a quarter of a circumference and performing four revolutions of $\frac{\pi}{2}$ to obtain a hemisphere, as shown in appendix A.0.1. This technique was adopted to avoid generating any unwanted asymmetries. Only the lower part of the sphere, i.e., the part below the mean free-surface, is discretized, consistently with linear theory. Regarding the list of frequencies, it was

calculated considering wavelengths that vary from 0.1 times to 100 times the diameter of the sphere, so calculating the wave number $k = \frac{2\pi}{\lambda}$ and consequently the frequency (using deep-water dispersion relationship) $\omega = \sqrt{gk}$. Once obtained the minimum and maximum frequency all the others are evaluated using a step of 0.05 between one frequency and the next. The problem was also solved at zero and infinite frequency.

The phase of the software validation involves a comparison of the obtained results with experimental tests on the free decay of a sphere [15]. A spherical shape was selected due to its geometric similarity to the CorPower WEC. Neither structure is wall-sided, and both demonstrate significant changes in their horizontal cross-sections. In these experiments, the sphere is released from three different heights in calm-water conditions, and the resulting heave motion is analyzed in the time domain. The goal is to assess the accuracy of the computational model by comparing its predictions against the observed behavior of the sphere in free decay.

To initiate this validation phase, simulations were carried out using both structured and unstructured meshes given as input to FFLOB together with a list of frequencies in order to run a convergence study to identify the geometry discretization with a sufficient number of panels to obtain stable results without exceeding to avoid to inflate the time needed to perform the simulation. As anticipated the fundamental difference between the two types of meshes lies in the arrangement of grid points, with structured meshes adopting an organized, grid-like structure, and unstructured meshes offering more flexibility with irregularly arranged nodes. For both types of meshes, the panel count was increased, starting from N = 500, and progressing to 2000 and 3000 as shown in fig. 6.1 and fig. 6.2. Since it is assumed that halph of the sphere is submerged, consistently it is possible to note the meshes were computed only for half of the sphere since the solution in the frequency domain is fully linear and it solves the problem around the mean wetted surface in steady-state conditions, so the upper part of the surface piercing sphere outside of the water is not needed and it will be only included in the time domain solver when is needed to account of the dynamic pressure on the instant wetted surface. As already explained this process aimed to determine the optimal mesh configuration by examining the behavior of the solutions at different panel counts so the goal was to identify the most suitable mesh, along with the corresponding number of panels, for conducting simulations in the time domain to be compared with the experimental results.

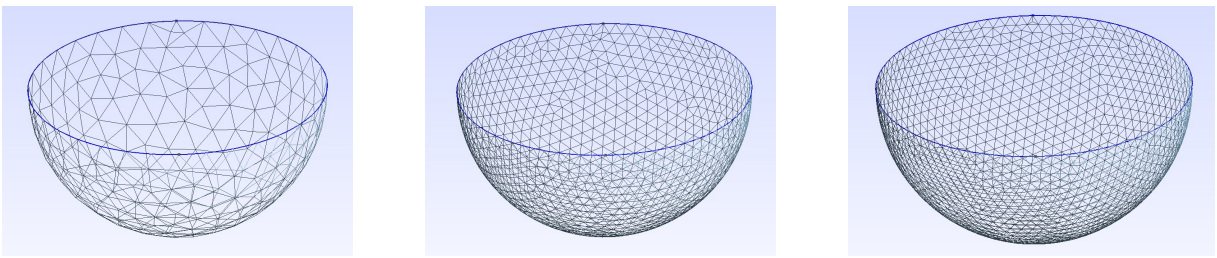

Figure 6.1: Unstructured meshes with 500, 2000 and 3000 panels from left to right

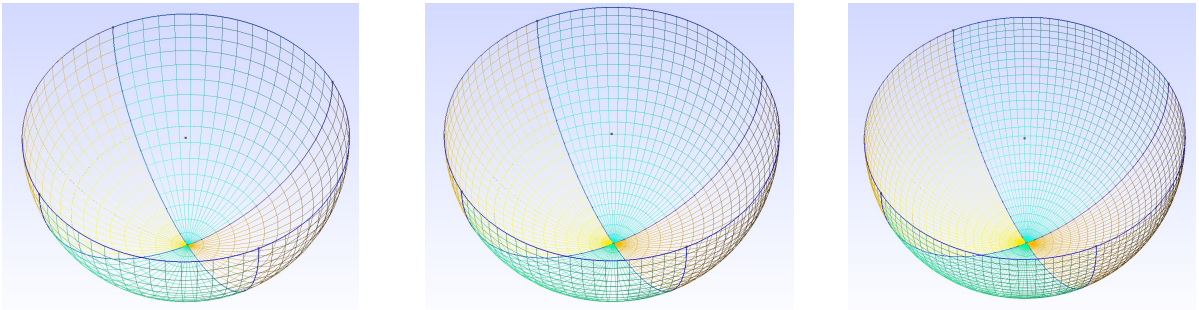

Figure 6.2: Structured meshes with 500, 2000 and 3000 panels from left to right

## 6.3 Numerical convergence for the sphere: frequency domain results

The convergence of results in the frequency domain is demonstrated by systematically increasing the number of panels for both the structured and unstructured meshes. The following graphs depicted in fig. 6.3 fig. 6.4 and fig. 6.5 represent the added mass, damping, and response amplitude operator curves computed through the frequency domain solver as previously explained. As the panel count is increased, the plots reveal how these key parameters converge enabling the selection of a mesh with a specific number of panels that yields accurate results without unnecessarily inflating the simulation time.

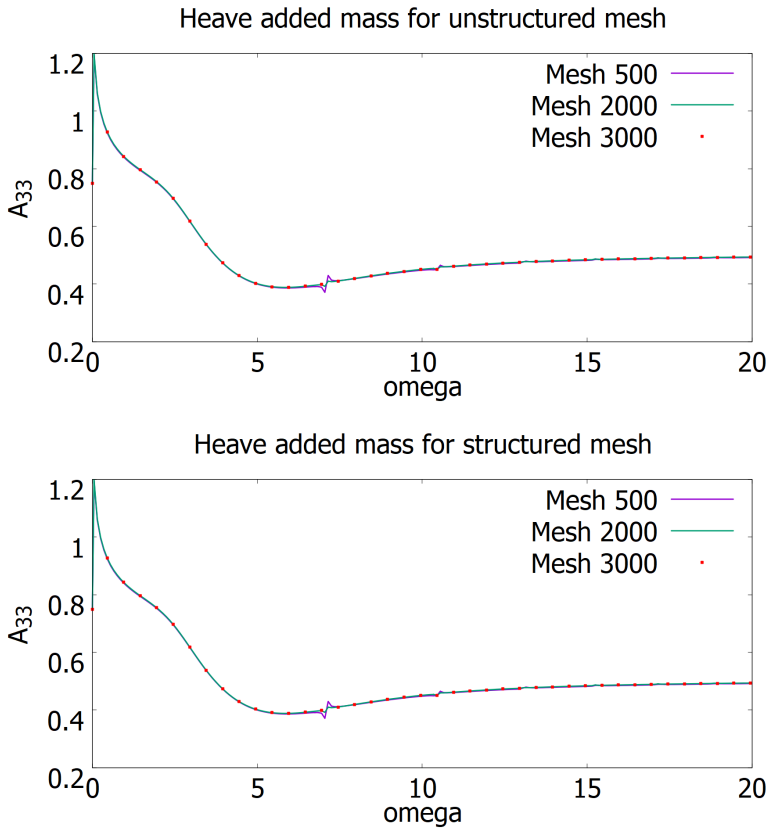


Figure 6.3: Adimendional Heave added mass for structured and non structured meshes as function of the frequency [Hz]

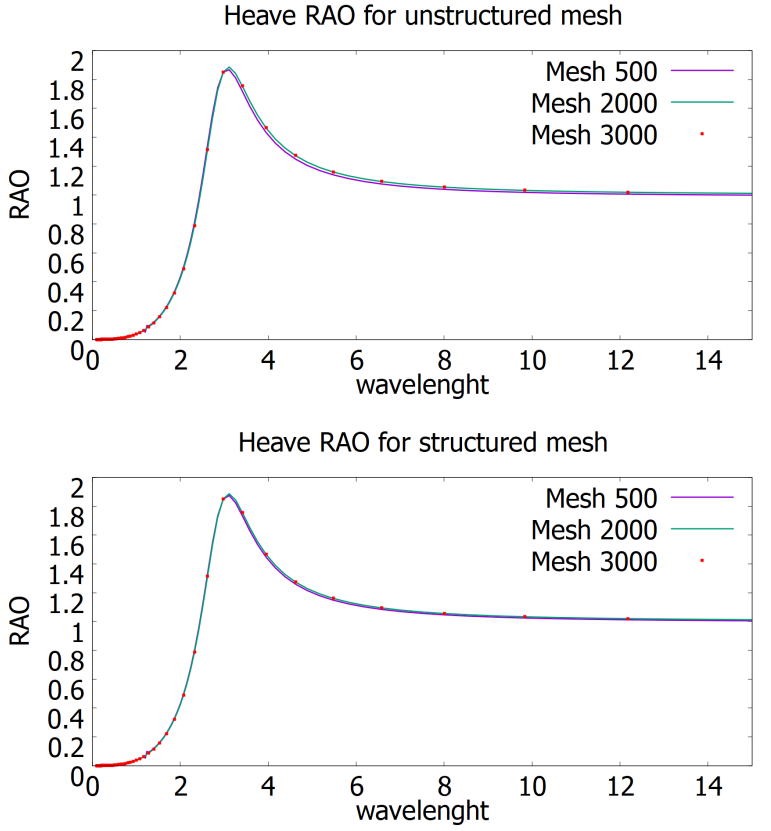


Figure 6.5: RAO for structured and non structured meshes as function of the wavlenght [m]

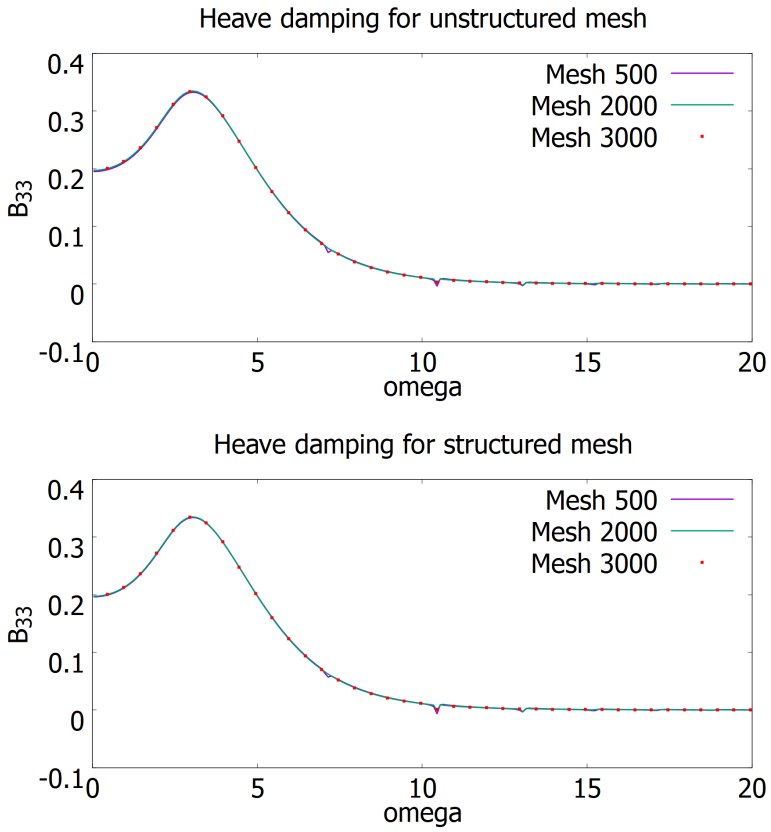


Figure 6.4: Adimensional Heave damping for structured and non structured meshes as function of the frequency [Hz]

It is evident that the results converge and demonstrate consistency for both the 2000 and 3000 panels meshes that also reduce the peaks of the irregular frequencies (more evident with the N = 500 mesh), unexpected deviations in the curves, mitigated increasing the mesh resolution, leading to a smoother curve as the number of panels increase, thus validating their utilization in conducting the time domain analysis.

## 6.4 Influence of draft on added mass

Before dvelving in the time domain analysis it is performed a study of draft's influence on added mass, interesting in bodies with a steep change in cross-section, such as spheres, offers an insights into the hydrodynamic behavior of this body. This study has been performed for understanding how similar geometric traits as the sphere can be compared with the WEC analysed later, since they both share this steep cross-sectional variation.

To perform this analysis the added mass at infinite frequency was calculated with FFLOB at different draft values of a sphere with 0.15 m radius. The results represented in fig. 6.6 are normalized with respect to the added mass calculated at half of the sphere submerged and the radius of the sphere respectively.

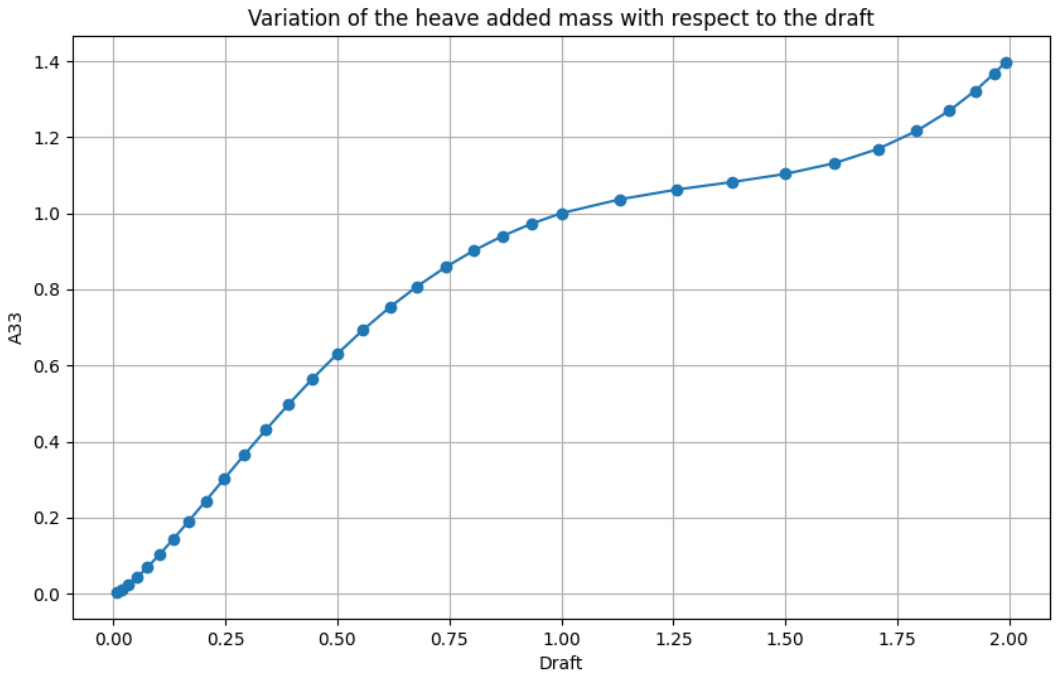


Figure 6.6: Variation of the heave added mass as function of the draft

In the time domain solution adopted for this studies, the added mass is not changing with the different values of the draft varying during time but is taken at infinite frequency and calculated at the mean expected draft as in eq. (4.27).

## 6.5 Free-decay time domain analysis and results

As mentioned earlier, the results obtained from free decay simulations in time domain were compared with experimental tests that analyze the heave motion of a sphere dropped into water from three different heights: 0.1D, 0.3D, and 0.5D, with the diameter of the sphere in the experimental results equal to 0.3m and the one of the simulation, whose results are properly scaled, equal to 1m. Free decay refers to the motion of an object, in this case, the sphere, experiencing oscillations in calm-water conditions without external forces. The fig. 6.7 below presents the results of the experimental tests obtained for the three different heights.

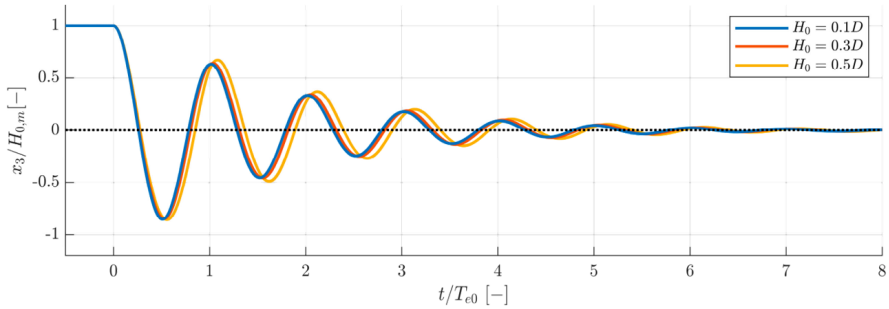


Figure 6.7: Free decay experimental results

All the results are dimensionless. In particular the time is normalized with the damped natural period in heave, (calculated using the hydrodynamic coefficients for the statically neutrally buoyant position) $T_{e0} = 0.76s$ of the sphere and the heave motion is divided by the initial height from which the sphere is dropped. As evident from the results of the simulations obtained using an unstructured mesh with 2000 panels in both the linear solution and in the one accounting of the nonlinearities stated in points 1 and 2 of section 4.5, an increase in the initial height from which the sphere is dropped reveals a growing differences between the two solutions. Those effects become more pronounced as the amplitude of motion grows, leading to deviations from linear predictions as shown in fig. 6.8. As already anticipated, to integrate the nonlinear effects also the upper part of the sphere geometry was discretized in the same way of the lower part and given as input to the time domain solver. It has been decided to incorporate these two nonlinear effects rather than viscous forces because flow separation in viscous effects is a phenomenon that requires time, larger motions, and velocities. Indeed, by making an approximate estimate of the KC number, calculated as $\frac{2\pi a}{D}$ where a is the maximum motion amplitude (0.5D), it results in being less than 4. Therefore, viscous effects are very unlikely to be significant in this free decay case, in addition to being of more complex implementation.

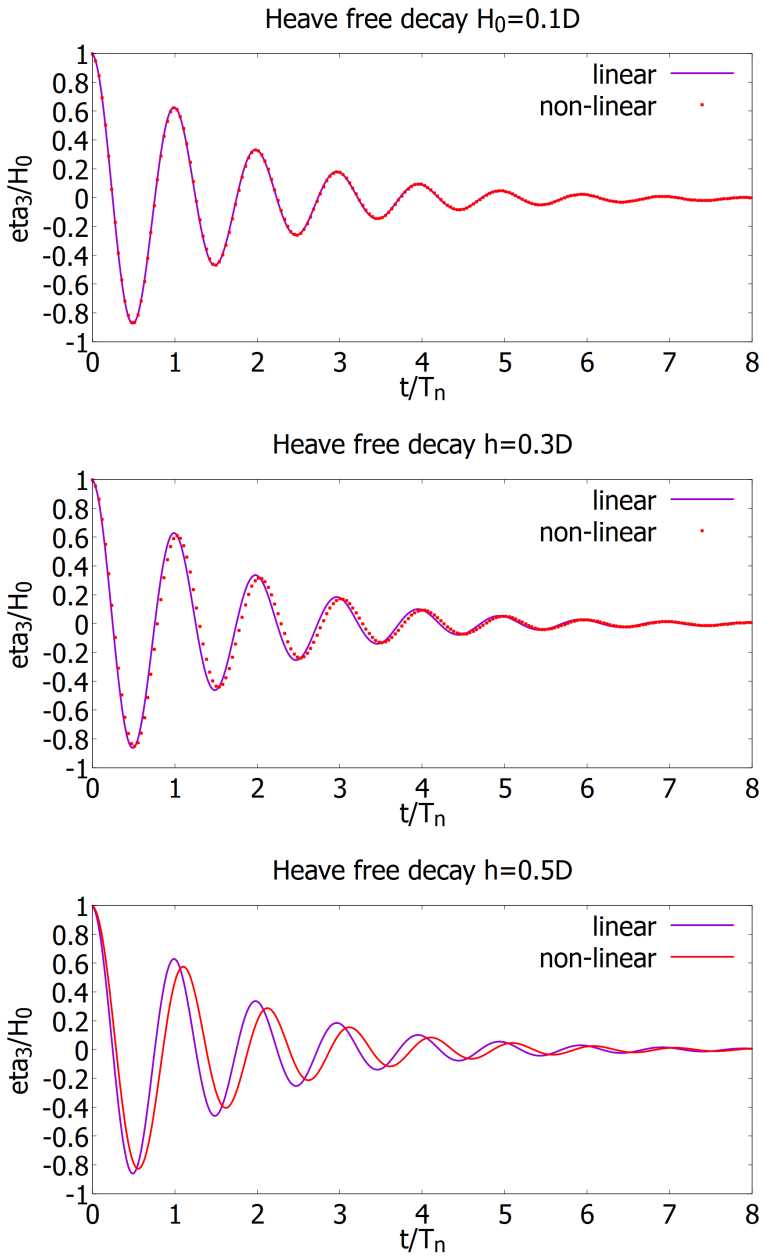


Figure 6.8: Comparison between linear and non-linear results for the three cases

In the same way, the results obtained with a sphere using 3000 panels remain consistent with those attained earlier, as depicted in fig. 6.9.

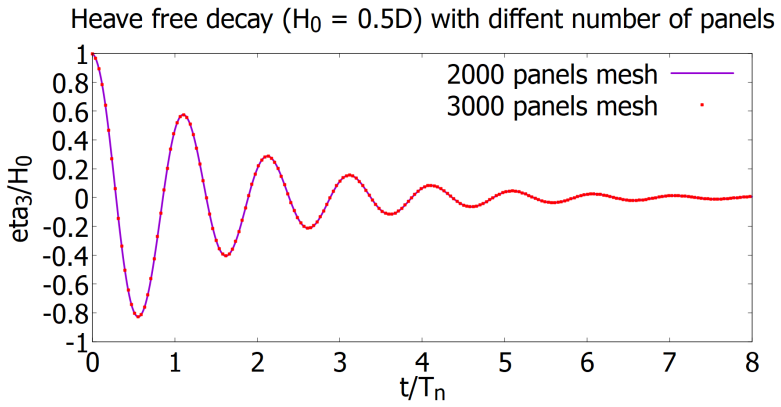


Figure 6.9: Comparison with more panels

This uniformity also persists whether an unstructured or structured mesh is employed as shown in fig. 6.10.

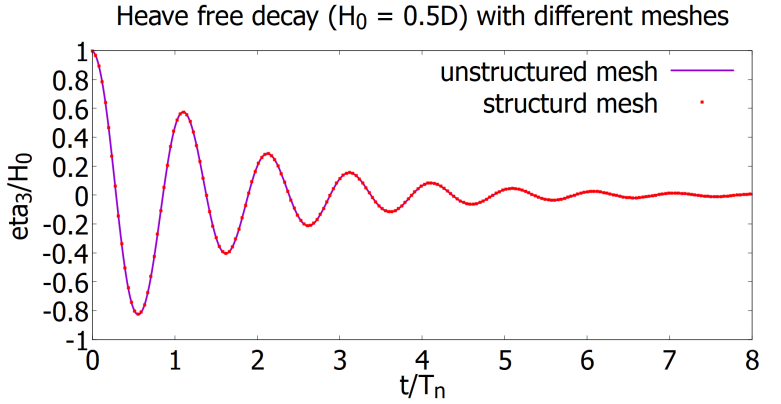


Figure 6.10: Comparison between structured and unstructured meshes

However, by analyzing the sway and surge motions showed in fig. 6.11 for both a structured and an unstructured sphere, it becomes apparent that the results with a structured mesh preserve better the symmetry of the body. This is because an unstructured mesh introduces unintended asymmetries. Therefore, considering the symmetry of the point absorber C4 geometry with respect to the z-axis, a structured mesh will be employed for simulations related to the Wave Energy Converter (WEC). This decision is driven by the structured mesh's ability to better capture the symmetrical characteristics of the system, avoiding undesired asymmetries introduced by the unstructured mesh, thus enhancing the overall precision of the simulations.

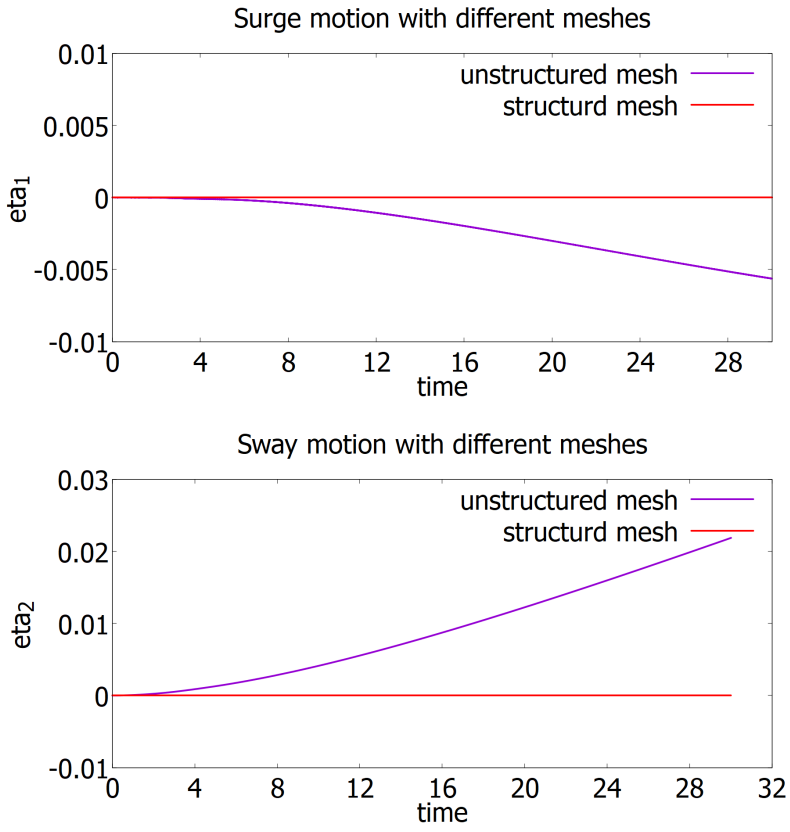


Figure 6.11: Surge and sway motions with different meshes

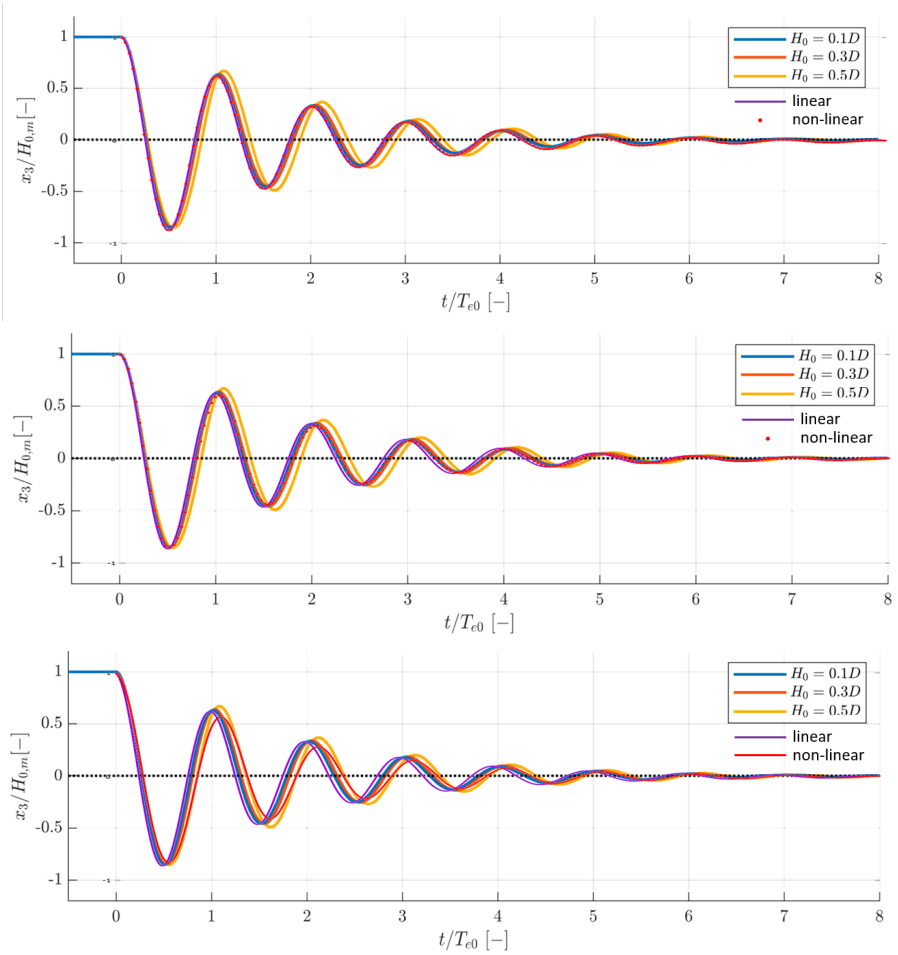


Figure 6.12: Comparison between the experimental data and the simulation performed with $H_0 = 0.5D$ and structured mesh

Comparing the results of the experimental tests with the ones of the simulation with the structured mesh and with an initial height of 0.5D, in fig. 6.12, it is evident that the outcomes are consistent in terms of change of oscillation (natural) period of the sphere and they are mostly due to nonlinear hydrostatic effects so once the software is validated it is possible to move on to the analisys of the CorPower WEC.

# Chapter 7

# Analysis of WEC C4

Regarding the studies conducted with CorPower's WEC C4, an equivalent system to that developed by CorPower to carry out experimental trials in the COAST laboratory at Plymouth University, was developed. The system of the experiments is a 1:25 scale model consisting of the WEC hull directly connected to the moorings without the presence of the PTO (infinite stiffness) and the slide on which the buoy can move (as in the final design realized by CorPower) thus obtaining a similar model to the detuned case for storm protection where the PTO stiffness is significantly high, leading to a reduction in heave motion. The moorings themselves consist of three parts and were modeled for simulations as two springs in series with their equivalent axial and torsional stiffness. To summarize, the behavior of this model in water can be likened to that of an inverted pendulum composed of a buoy and a spring, i.e., the moorings, which have the ability to rotate just like a pendulum thanks to an H-link joint with the moorings that allows for rotations.

(a) Full-scale WEC

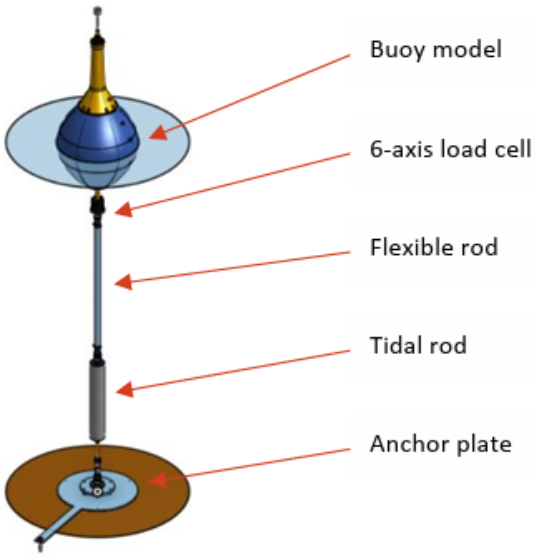


(b) Model of the WEC (scale 1:25)

Some of the WEC's features have been detailed in chapter 3, and all simulations were conducted at full scale, leveraging the experiment results from CorPower's scaled model, which have been upscaled to full scale. Due to the sensitive nature of the geometry data, further specifics cannot be shared.

The plots in this chapter, providing dimensional quantities, give their dimensions in the SI units.

## 7.1 Modeling of the hull of the WEC

Same as the case of the sphere for the verification phase, a structured mesh was also created for the geometry of the CorPower floating buoy with 4 revolutions of the profile. As can be seen from the script in appendix A.0.2, a spline was created to join a series of points combined with lines to define the stepped profile part of the buoy. The three meshes with an increasing number of panels to conduct an initial convergence study in the frequency domain are shown in fig. 7.2, the results of which are analyzed in the following paragraph. Also in this case, only the mesh of the submerged part of the WEC hull in its average configuration was given as input to FFLOB, along with the file of calculated frequencies, always considering waves with a length from 0.1 to 100 times the diameter of the buoy. An initial analysis using three meshes of 500, 1000, and 2000 panels, respectively, as shown in the figure, was conducted to examine the convergence of the added mass, damping, and Response Amplitude Operators (RAO).

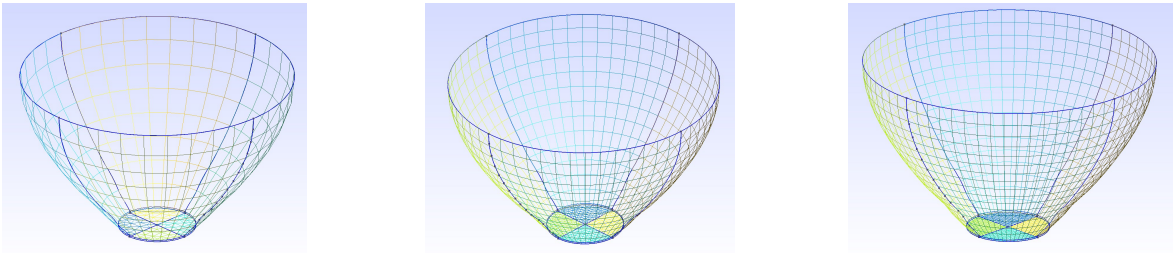

Figure 7.2: 500, 1000 and 2000 panels structured meshes of the WEC

## 7.2 Numerical convergence for the WEC: frequency domain results

Below, the results for added mass, damping, and Response Amplitude Operators (RAO) for heave motion are shown. It is important to highlight that the results of these simulations cannot be used to analyze the response of the complete system, as the full system is not considered, notably lacking the moorings. Therefore, the obtained results are necessary only for conducting a convergence study to analyze the sufficient number of panels required to discretize the geometry of the body.

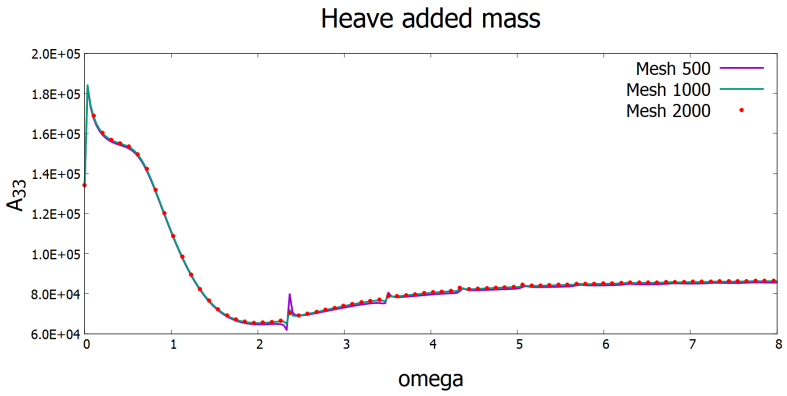


Figure 7.3: Heave added mass for the WEC

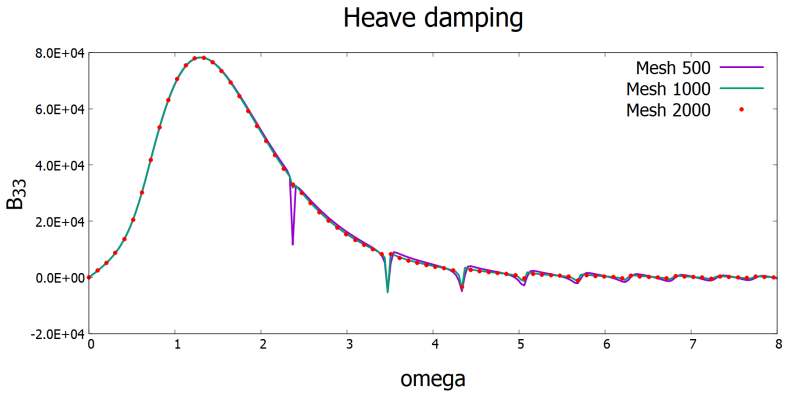


Figure 7.4: Heave damping for the WEC

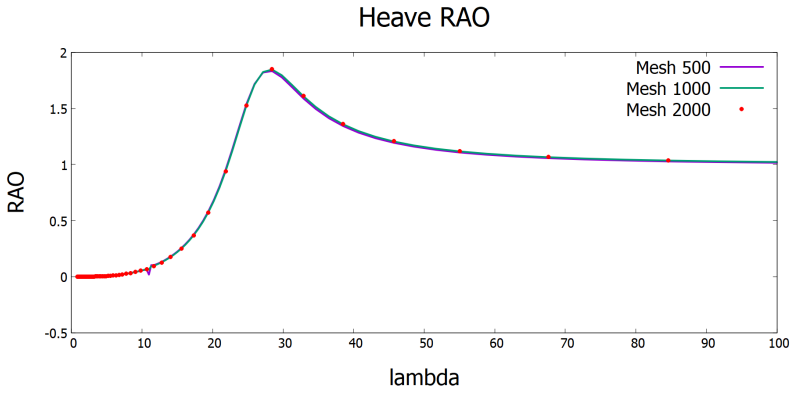


Figure 7.5: Heave RAO for the WEC

As can be observed from the figures, the mesh with 1000 panels is sufficient to solve the problem with an adequate degree of precision also reducing the peaks of the irregular frequencies. Moreover it is interesting to notice that the maximum value of the RAO for the WEC it is similar to the one of the sphere in section 6.3.

## 7.3 Influence of draft on hydrostatic restoring, added mass and natural period

As already discussed in the chapter on the frequency domain solver FFLOB, the problem is solved in a steady-state condition, and consequently, the results obtained are significant for submersion around an average configuration. Also within linear theory there are motions but due to the geometry small vertical motions can lead to large changes in the hydrostatic and added mass effects and here a quasi-static approach is used to check this and the features of the geometry. So a study on the variation of hydrostatic restoring, added mass and natural period in heave as a function of the body's submersion was conducted. To accomplish this, it was necessary to recreate the different geometries of the submerged body to provide as input to FFLOB, and as shown in fig. 7.6, 4 new configurations were taken in addition to the one already used previously.

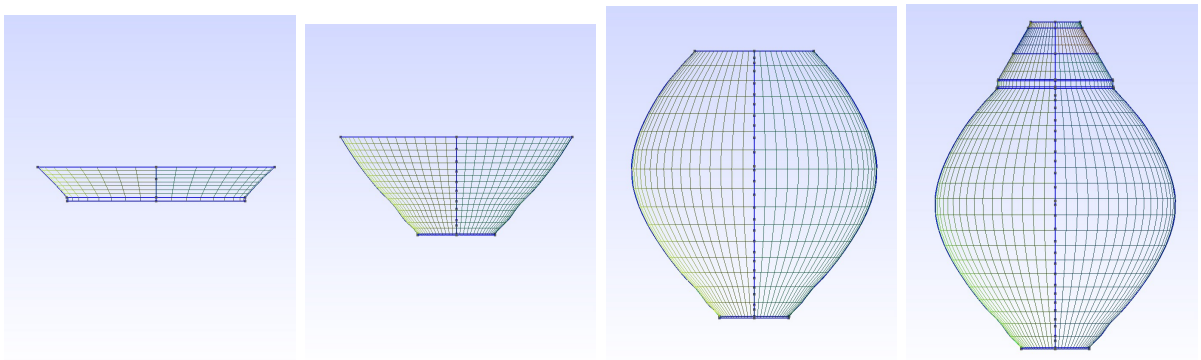

(a) (b) (c) (d)

Figure 7.6: Meshes with different draft values: a) 0.49m b) 3.25m c) 8.89m d) 12.4m

Using $C_{33}(D)$ and $A_{33}(\omega, D)$ associated with the actual submerged structure, it is possible to examine the influence on the natural frequency in heave $\omega_{3n}$, assuming a 1DOF (One Degree of Freedom) undamped system. In this scenario, $\omega_{3n}$ can be estimated as the frequency where the two curves $y = C_{33}(D)$ and $y = \omega^2(M + A_{33}(\omega, D))$ intersect,

$$\rho g \pi r^2 = \omega_n^2 [M + A_{33}(\omega_n)] \tag{7.1}$$

Solving for $\omega_n$ provides the natural frequency of the system, offering valuable insights into its resonant condition.

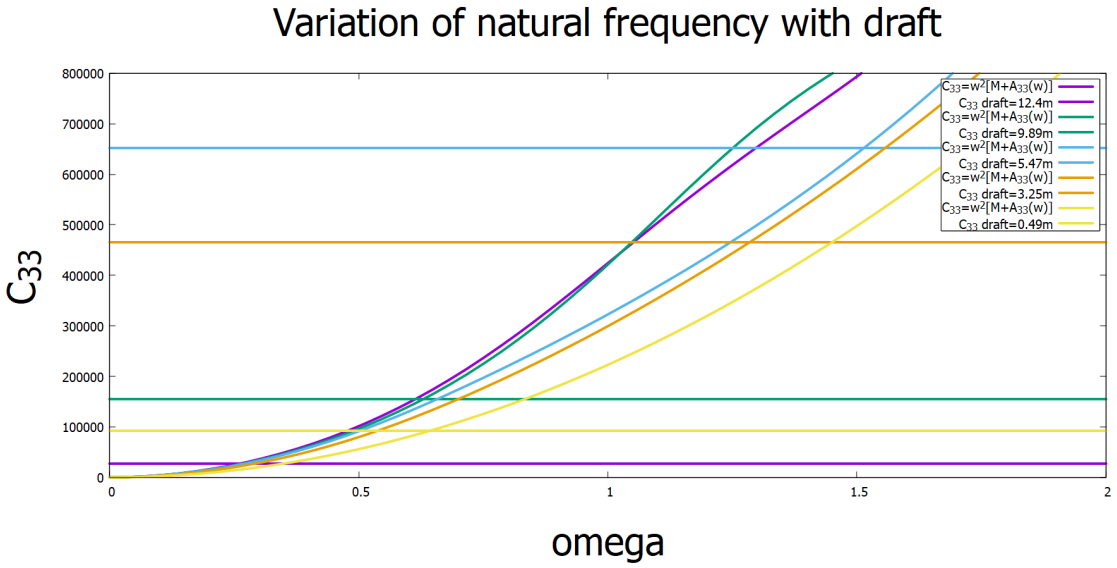


Figure 7.7: Influence of the draft on the natural frequency

The results of this analysis are shown in fig. 7.7 and it is possible to calculate the variation of the natural period of the WEC with different values of draft shown in table 7.1

| Draft (m) | $T_n$ (s) |
|---|---|
| 12.4 | 24.16 |
| 8.89 | 9.97 |
| 5.47 | 4.16 |
| 3.25 | 4.88 |
| 0.49 | 9.81 |

Table 7.1: Table of Natural Periods at Various Drafts

A plot of the interpolated values of the natural period as function of the draft is represented in fig. 7.8, evaluated as it can be seen in the script in appendix A.0.3.

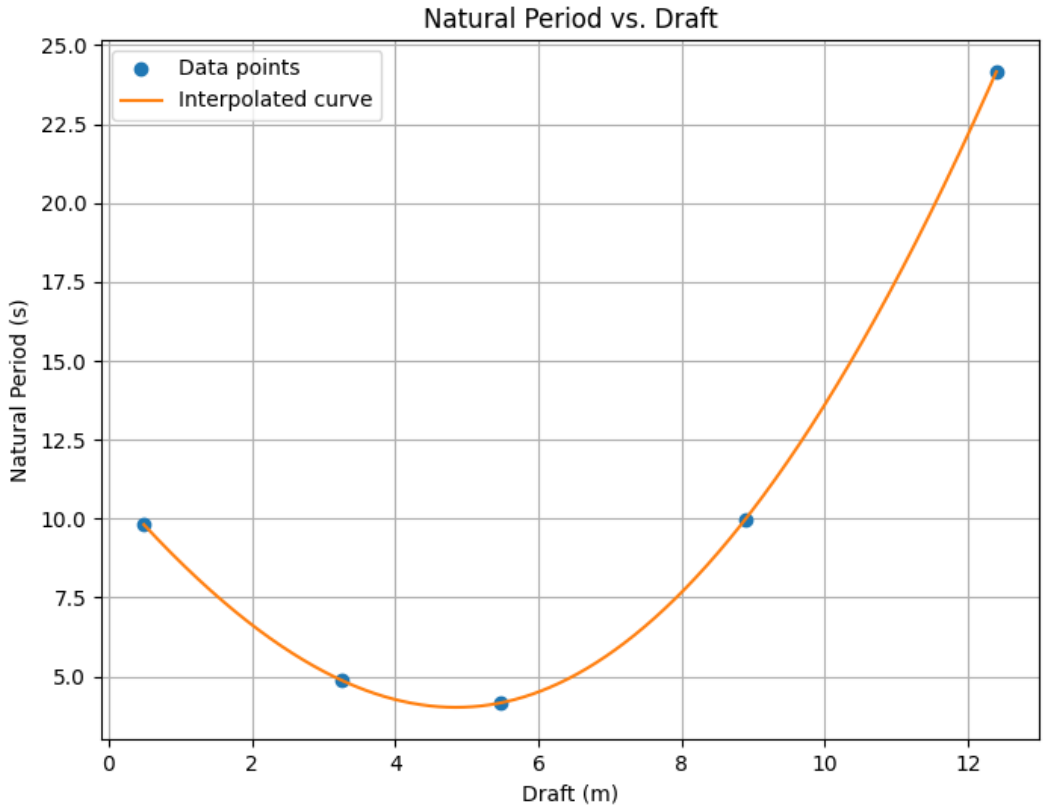


Figure 7.8: Influence of the draft on the natural frequency

The heave added mass results for the different draft values are shown in fig. 7.9. As expected, the added mass increases with the draft and, therefore, with the submerged volume.

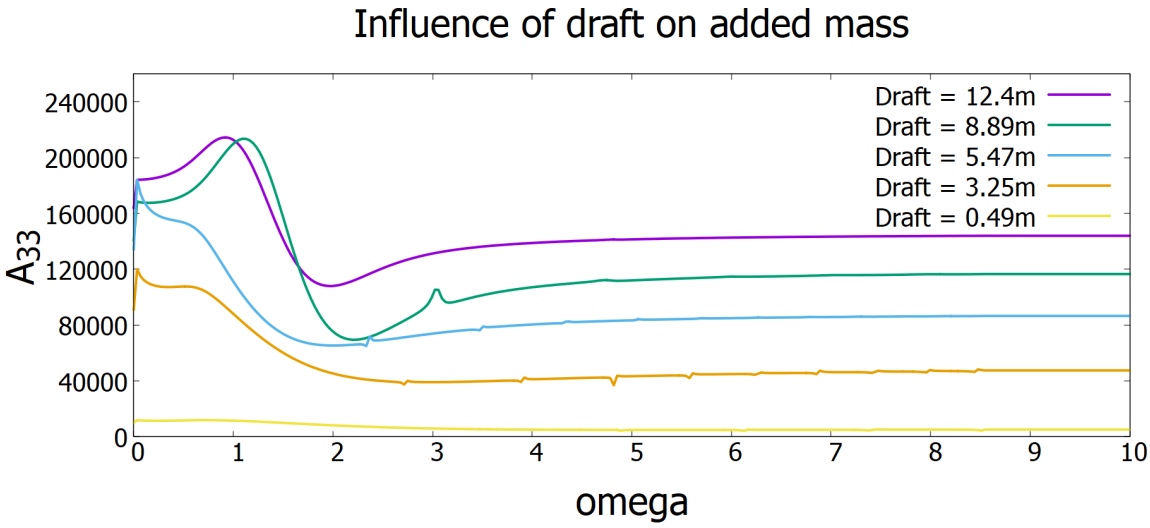


Figure 7.9: Influence of draft on heave added mass

Finally, the values of the added mass at infinite frequency as a function of draft were interpolated using a Lagrange polynomial, as shown in the script in appendix A.0.4 and in fig. 7.10, allowing a better understanding of the variation of this term with respect to the draft. Also the adimensional heave added mass is represented in fig. 7.11 where the added mass is divided by its value at usual draft to normalize it.

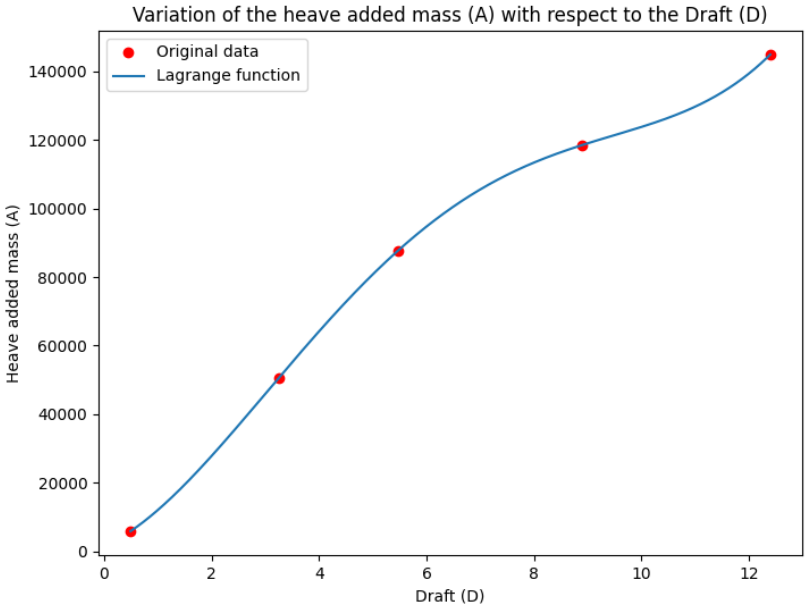


Figure 7.10: Heave added mass as function of the draft

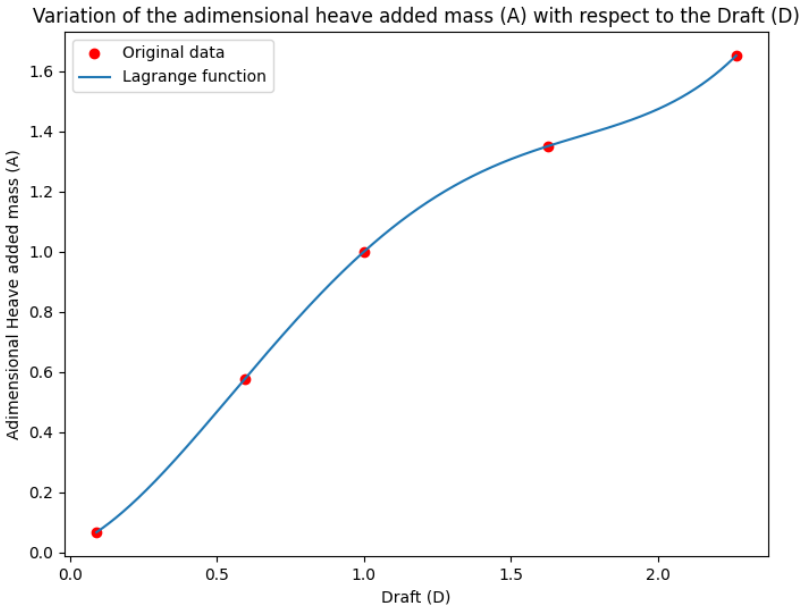


Figure 7.11: Adimensional Heave added mass as function of the adimensional draft

The results in fig. 7.11 were normalized in order to be compared with the one obtained in the case of the sphere in section 6.4. It is possible to note from the comparison that there is an interesting similarity between the two geometries due to the fact that both bodies present a steep variation of the cross-sectional area with the draft.

It is also important to note that the variation of this term is significant, although it must be emphasized that some configurations are particularly extreme and difficult to achieve. In any case, a correction associated with this could be introduced in the hydrodynamic loads, through using a quasi-static approach. In particular, one could consider the variation of the added mass in the software as a function of the draft and, therefore, as function of time , this could be done for the added-mass at infinite frequency only. Such correction would keep the solution strategy efficient and represents a more important contribution with respect to changes in the retardation function eq. (4.27), based on the work by [17]. However, in this study, it is only used the value of the added mass as seen in the Cummins' equation to perform the time domain simulations.

## 7.4 Time domain approach

As previously explained at the beginning of this chapter, the system can be likened to that of an inverted pendulum, consisting of a mass and a spring that can rotate together around the anchoring point on the seabed. For this reason, the heave and surge motions discussed in the results are a consequence of the rotation around the anchoring point and the projection of the buoy's position onto the z and x axes.

Additionally, the extension of the spring can also cause motion, but due to the high stiffness, this effect will not be particularly pronounced.

Regarding the simulations performed in the time domain, the procedure was as follows:

- The moorings were modeled as previously described at the beginning of the chapter, equivalent to two springs in series, utilizing the corresponding torsional and axial stiffness. Flexural stiffness was not considered since, with the system being free to rotate around the anchoring point ideally without any friction, the only flexural moment that could arise is due to the friction of the moorings with the surrounding water flow, an analysis not conducted in this thesis study.

- The equations of motion for the WEC were reformulated to impose the rotational motion around the center of rotation, which is the anchorage on the seabed.

- All the geometrical properties of the system, namely mass, center of mass, moments of inertia of the WEC hull, and mooring components, were inputted into the solver in the time domain.

- A free-decay surge motion was simulated to be compared with another provided by CorPower in a report, which contained the result of an experimental trial and also their numerical simulation conducted with Simulink.
- Simulations were conducted with regular waves and also irregular sea states of various characteristics reflecting those of adverse sea states at the Aguçadoura site in Portugal.

## 7.5 Results in free-decay

As an initial approach, the linear problem was solved without considering nonlinear effects and viscous forces, as explained in the theoretical background. The system's initial conditions were set at -11.7 m in surge, which is the motion under analysis, and subsequently calculated -1.68 m in heave and -16.36° in pitch, considering a circular trajectory with the radius equal to the distance between the anchoring point and the system's center of mass. The result in the time domain of the pitch motion is shown below.

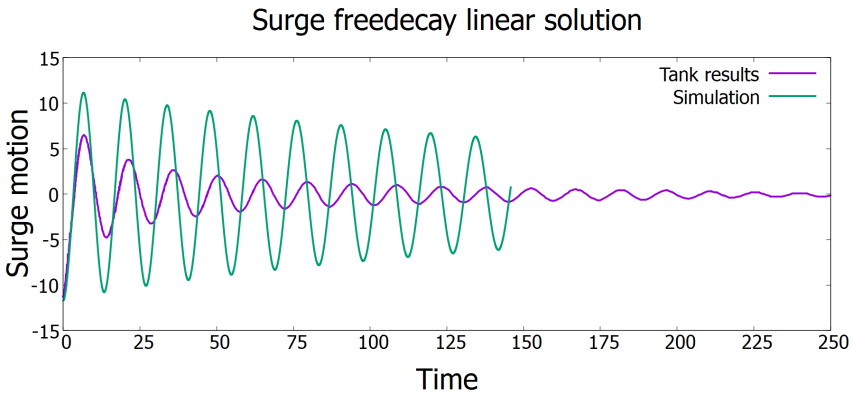


Figure 7.12: Linear solution of the surge free-decay

Comparing the results with the ones provided by CorPower's tank experiments, it is glamping the difference between both the decay (so the damping) and the oscillation period involved (so the natural period). In the simulation there is almost no damping and so the viscous forces through the Morison's equation will be modeled. Moreover it is possible to see that the simulation has a natural period of about 13.3 seconds compared to the 14.7 seconds of the experiments. Since the restoring effects are expected to be properly modelled, the reason of the disagreement should be checked in the added-mass effects. Indeed, until this point, the added mass term for the moorings has not been considered since it was not modeled in the input geometry of FFLOB that gives as output the added mass of the only buoy, and for this reason, it is calculated analytically through the strip theory as explained in Chapter 4.6 though the implementation of the viscous forces.

The system's diameter was determined as a function of the $s$ coordinate, as detailed in the Python script in appendix A.0.5 and illustrated in fig. 7.13

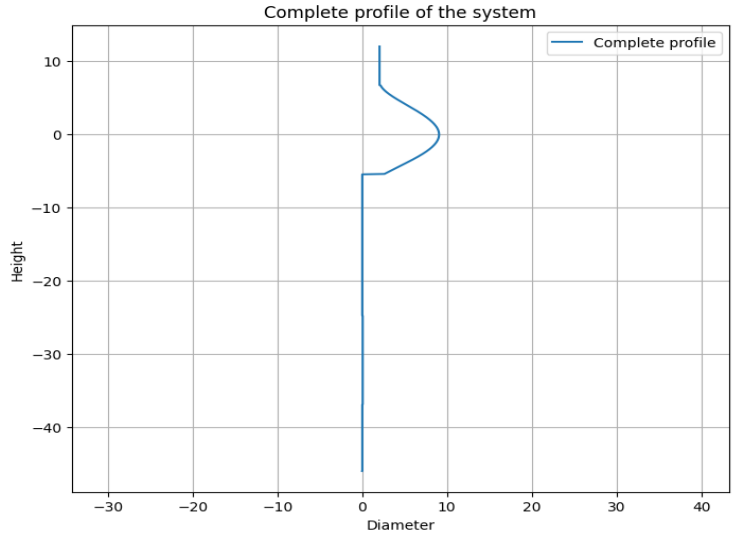


Figure 7.13: Diameter as function of the s vertical coordinate
values are in meters

The initial analysis encompassed three distinct scenarios. Consequently, the KC value varies with the $s$ coordinate of the moorings, leading to the selection of the following cases for the analysis:

1. With minimum KC, $C_a = 1$.
2. With maximum KC and minimum roughness, $C_a = 0.6$.
3. With maximum KC and maximum roughness, $C_a = 0.2$.

The outcomes for these three scenarios are depicted in the following figures:

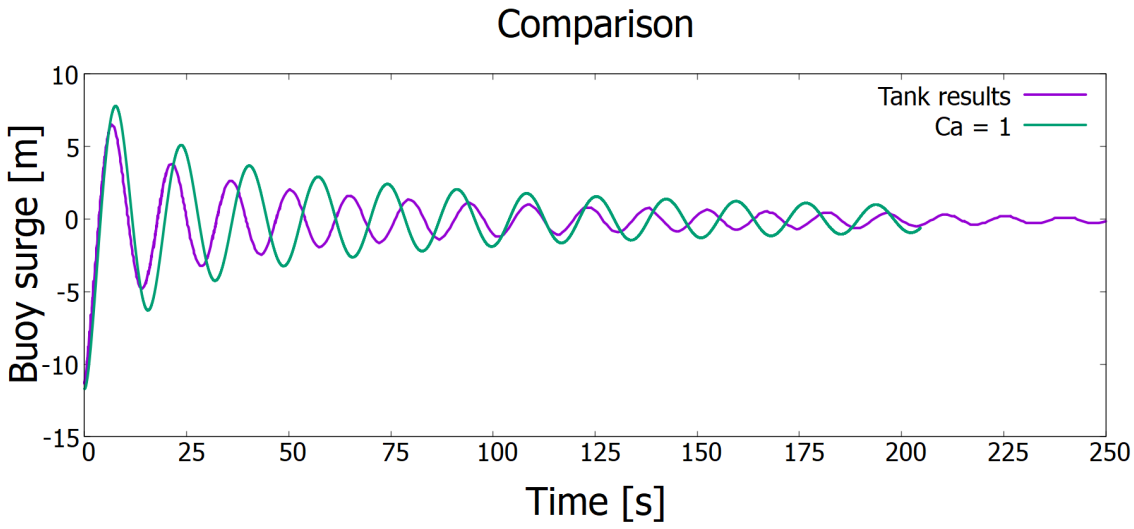


Figure 7.14: Surge free-decay comparison with $C_a = 1$

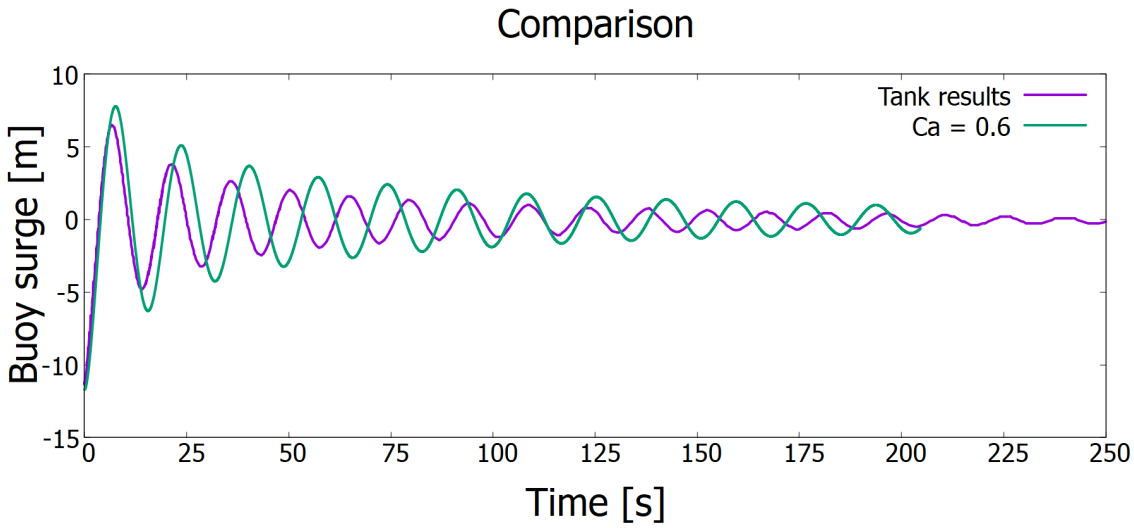


Figure 7.15: Surge free-decay comparison with $C_a = 0.6$

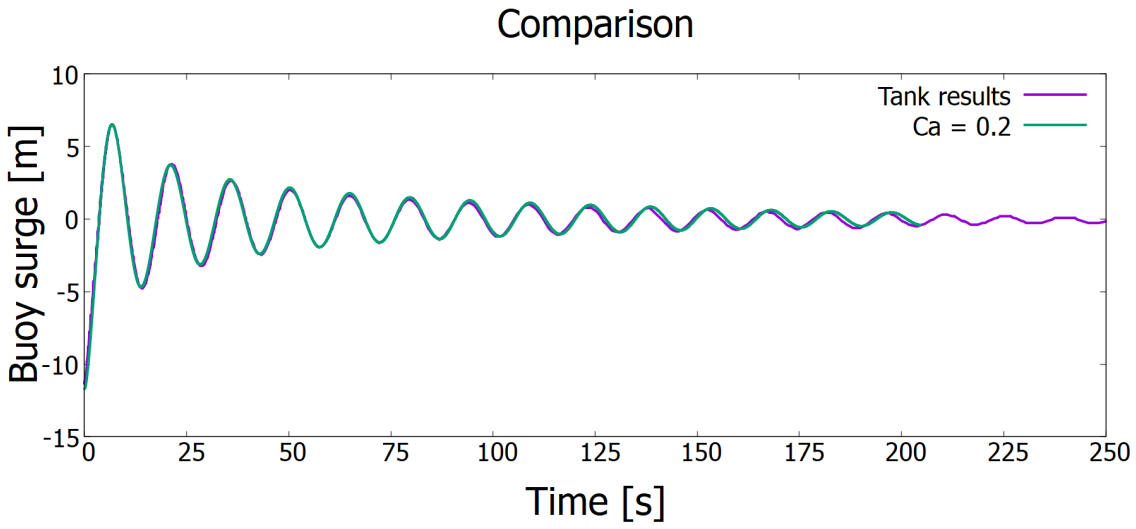


Figure 7.16: Surge free-decay comparison with $C_a = 0.2$

Analyzing the outcomes, it becomes evident that the solution most closely aligning with CorPower's experimental findings is characterized by a $C_a$ value of 0.2. This scenario is indicative of significant roughness alongside an elevated KC number. Notably, the calculated mean KC number, based on the structure and within the initial 40-second period of free decay, is approximately 21.26. Reference to the accompanying chart in fig. 4.4 confirms this observation, aligning with a Cm value of 1.2 and reaffirming a Ca value of 0.2, underscoring the coherence between the previous assumption and the roughly evaluated KC number.

## 7.6 Results in regular waves

In this section, the presented results are derived from simulations conducted with regular waves, marking a significant step towards understanding the device's behavior under controlled conditions. It is important to note, however, that a direct comparison with real-world data or reference datasets is currently not feasible due to the unavailability of such information. This limitation does not detract from the value of the simulations but highlights the need for further research and data collection to fully validate the model's predictions. The pursuit of additional data and comparative studies will be crucial for advancing our understanding and enhancing the reliability of those simulations.

Regarding the chosen cases, the operational range of the WEC, which is 0.25-8 meters in significant wave height (Hs), was taken into account. By approximating the wave height to be two-thirds of the significant wave height Hs, three scenarios were identified. Two fall within the operational range with wave heights of 2.6 meters and 5.3 meters, and one falls outside of this range with a wave height of 8 meters. Subsequently, considering the amplitudes of these three waves, the wavelength was calculated using a wave steepness

of 0.1. This value represents a threshold beyond which the nonlinear effects of the waves become more pronounced and within which the waves can be described in a linear context. The table 7.2 presents the parameters of the three waves studied.

| Wave n° | Hs (m) | H = (2/3 Hs) (m) | a (m) | $\lambda$ (m) | $k = \frac{2\pi}{\lambda}$ | $\omega$ (rad/s) | T (s) |
|---|---|---|---|---|---|---|---|
| 1 | 4 | 2.6 | 1.3 | 26.6 | 0.23 | 1.52 | 4.13 |
| 2 | 8 | 5.3 | 2.6 | 53.3 | 0.12 | 1.07 | 5.8 |
| 3 | 12 | 8 | 4 | 80 | 0.078 | 0.87 | 7.16 |

Table 7.2: Waves Parameters

The results for the three different cases for heave and surge motion are represented in fig. 7.17, fig. 7.18 and fig. 7.19. It is important to state again the heave and surge motion represented in those results are always the projection respectively on the z and x axis of the position of the center of mass of the buoy that is rotating around the anchoring point.

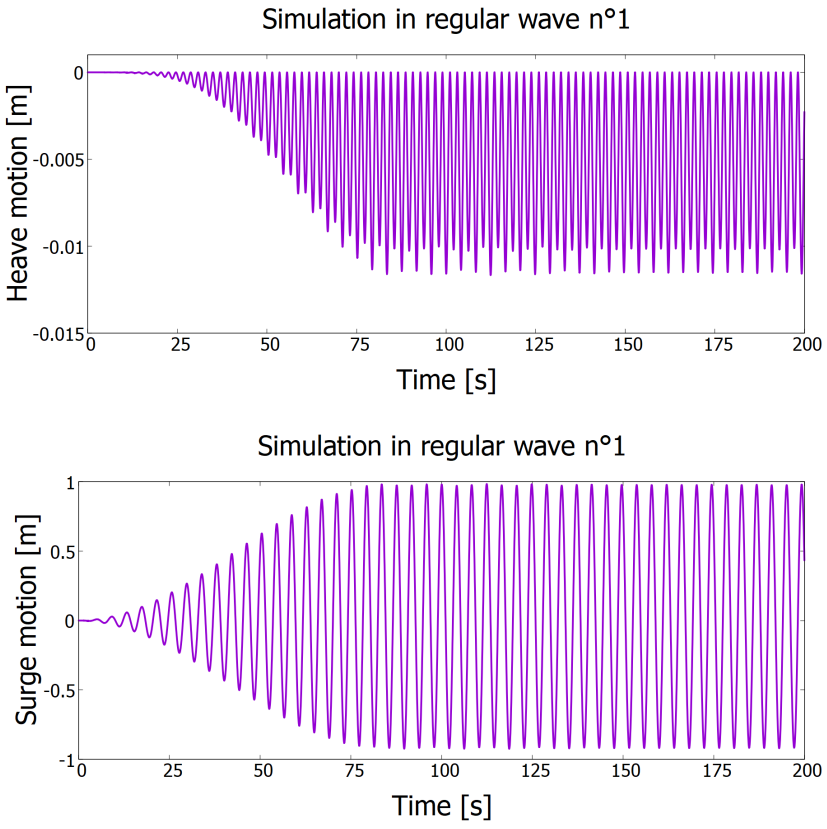


Figure 7.17: Surge and heave motion for regular wave n°1

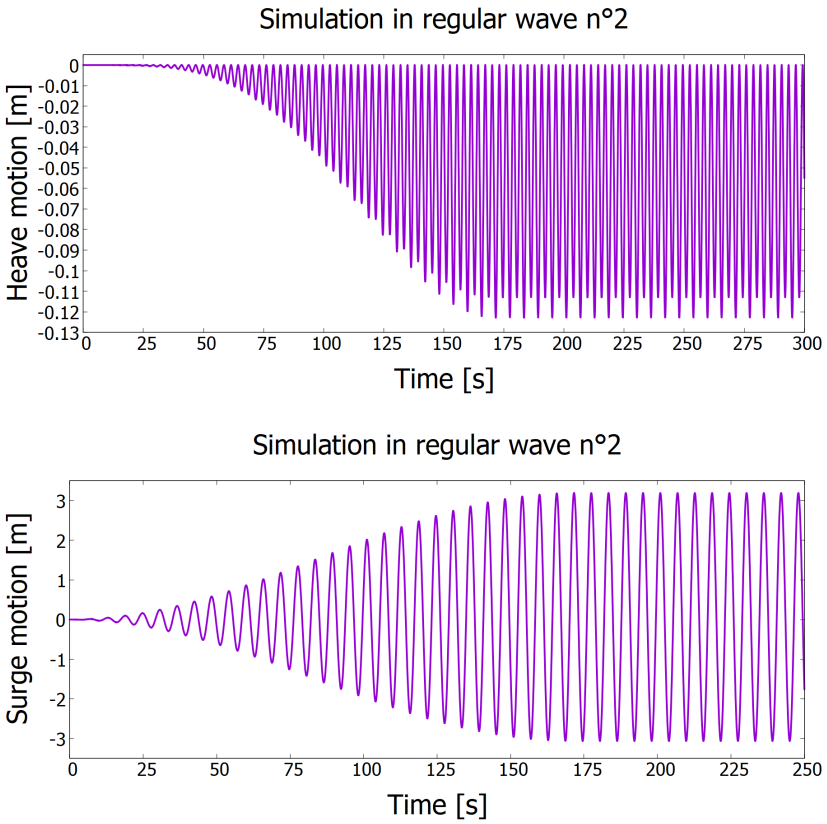


Figure 7.18: Surge and heave motion for regular wave n°2

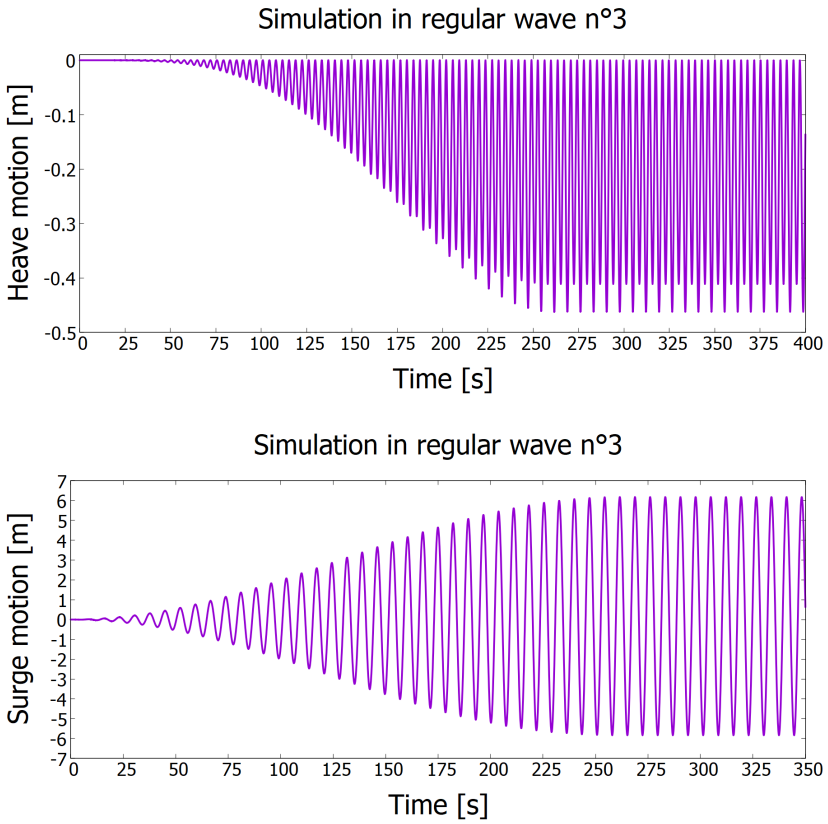


Figure 7.19: Surge and heave motion for regular wave n°3

All the graphs show a regular pattern, since the simulations were run with regular waves, where the amplitude and period are consistent over time after an initial transient. The heave motion oscillates between zero and negative values because the results were reported by shifting to a zero value the position of the center of mass when the system is in vertical equilibrium.

## 7.7 Results in irregular waves

Regarding irregular waves, simulations were conducted following the experimental results provided by CorPower to enable comparison. Specifically, simulations were carried out using irregular waves represented by the Jonswap spectrum, with the characteristics displayed in table 7.3.

| State n° | Hs (m) | Tp (s) | Wave spec. | $\gamma$ |
|---|---|---|---|---|
| SA4 | 9.51 | 13 | Jonswap | 1.7 |
| SA6 | 10 | 15 | Jonswap | 1.7 |

Table 7.3: Irregular Waves Parameters

Here Tp indicates the peak period and $\gamma$ is a parameter that describes the peakedness of the wave energy spectrum around its dominant frequency.

The results obtained with the model implemented in this study and the ones obtained by CorPower (including both tank and simulation results) are represented in fig. 7.20, fig. 7.21, fig. 7.22 and fig. 7.23.

Due to lack of information about the random phase (seed) that was used to create the irregular wave patterns, a direct temporal comparison of the results is impossible to perform. The wave time histories are not aligned, precluding a closer examination. Consequently, the comparison can only be generalized to observe the average oscillatory behavior of the heave motion and axial forces.

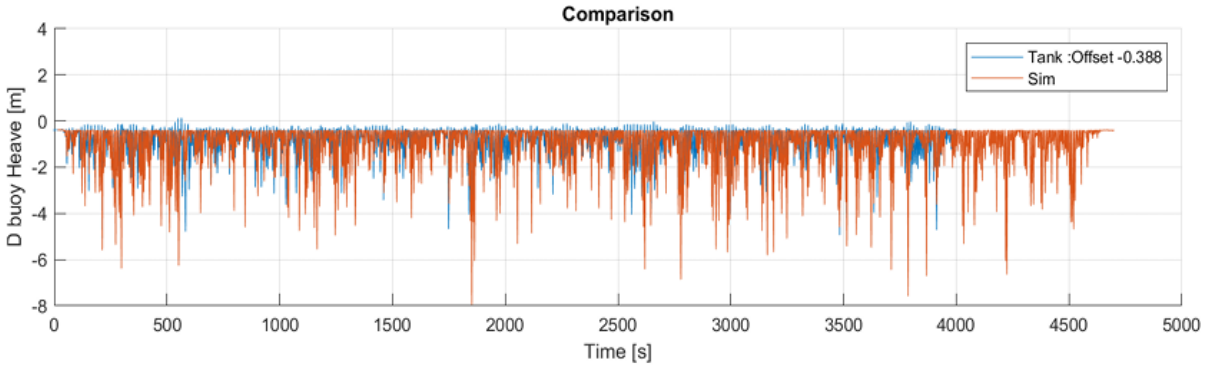


(a) Heave motion with irregular waves SA4

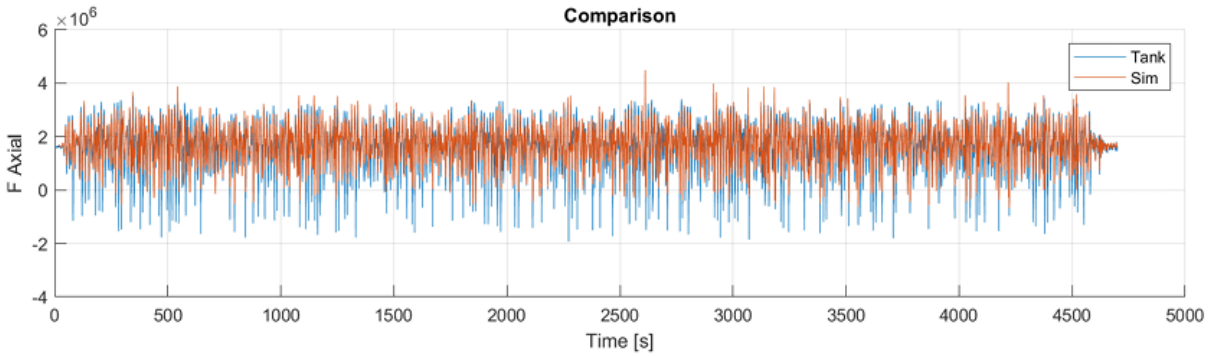


(b) Axial forces with irregular waves SA4

Figure 7.20: Heave motion and axial forces for both experimental and numerical simulations conducted by CorPower with irregular waves SA4

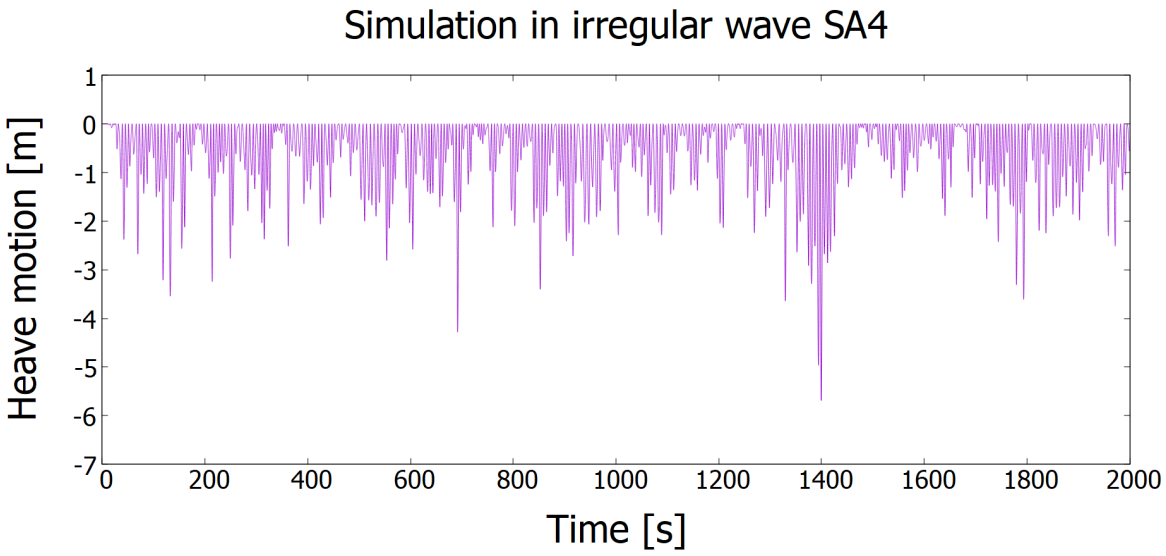


(a) Heave motion with irregular waves SA4

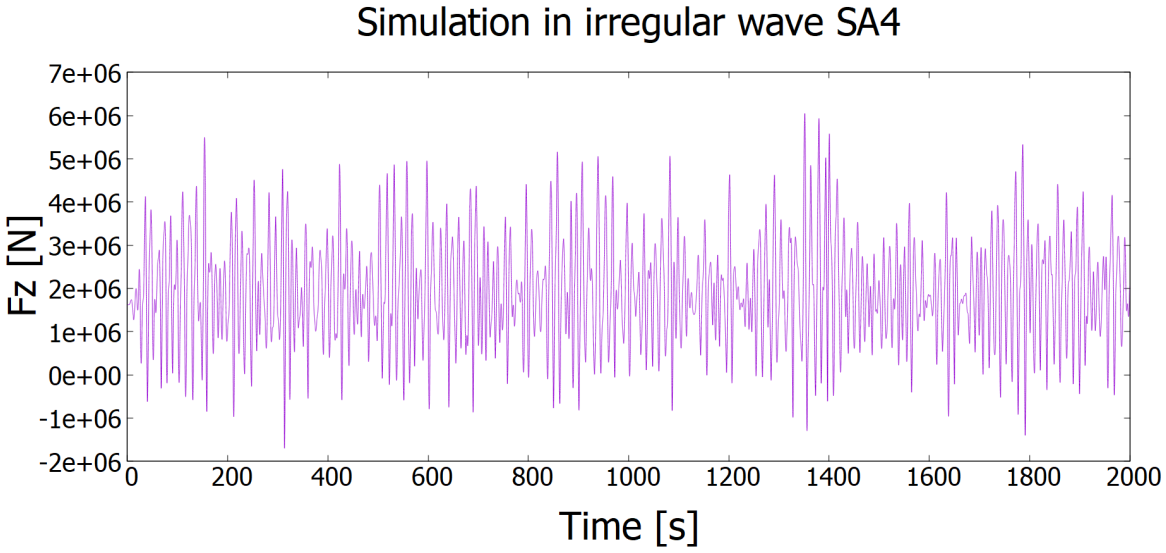


(b) z-component of the mooring forces with irregular waves SA4

Figure 7.21: Results of the simulations for heave motion and z-component of the mooring forces with irregular waves SA4

As it is possible to see in Figure 7.21a, the heave motion values oscillate between zero (as anticipated) and a minimum of -5.7 meters. Further, a statistical analysis reveals that the heave motion exceeds only once the threshold of 90% of this minimum value, and surpasses the 70% of the threshold three times. It is important to note that among these occurrences, the instance of the absolute minimum value itself is included.

In the same way it is possible to analyse the values of the z component of the mooring forces in fig. 7.21b and state that the maximum and minimum value are respectively

$6.047 \cdot 10^6 N$ and -$1.7 \cdot 10^6 N$. The negative values occurs when the wave trough is lower than the draft of the buoy that remains completely out of the water and so the moorings undergo a compression state. The threshold of 90% of the maximum value is exceeded 4 times in this time history.

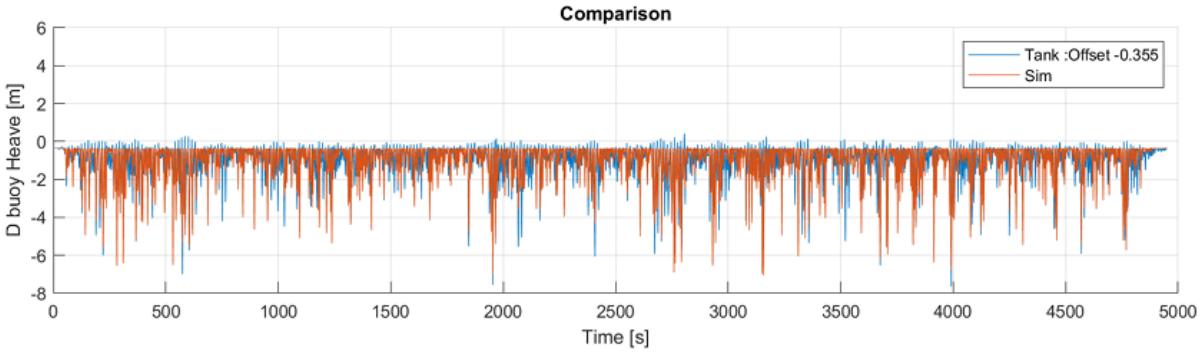


(a) Heave motion with irregular waves SA5

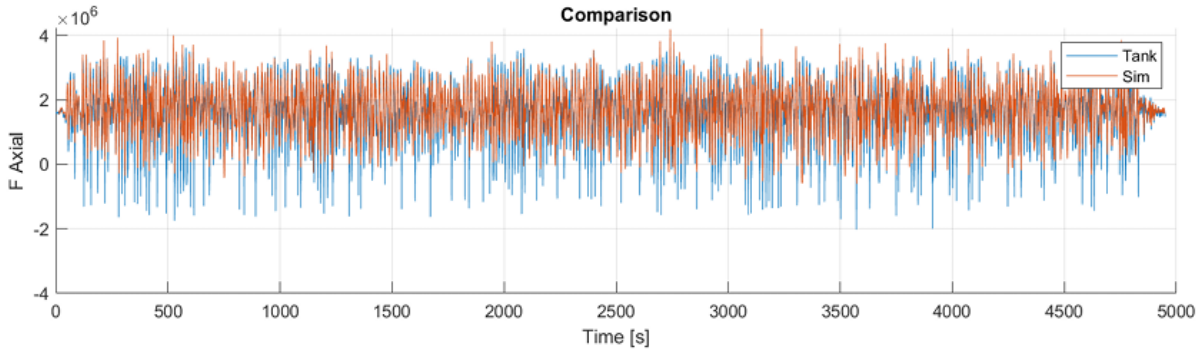


(b) Axial forces with irregular waves SA5

Figure 7.22: Heave motion and axial forces for both experimental and numerical simulations conducted by CorPower with irregular waves SA5

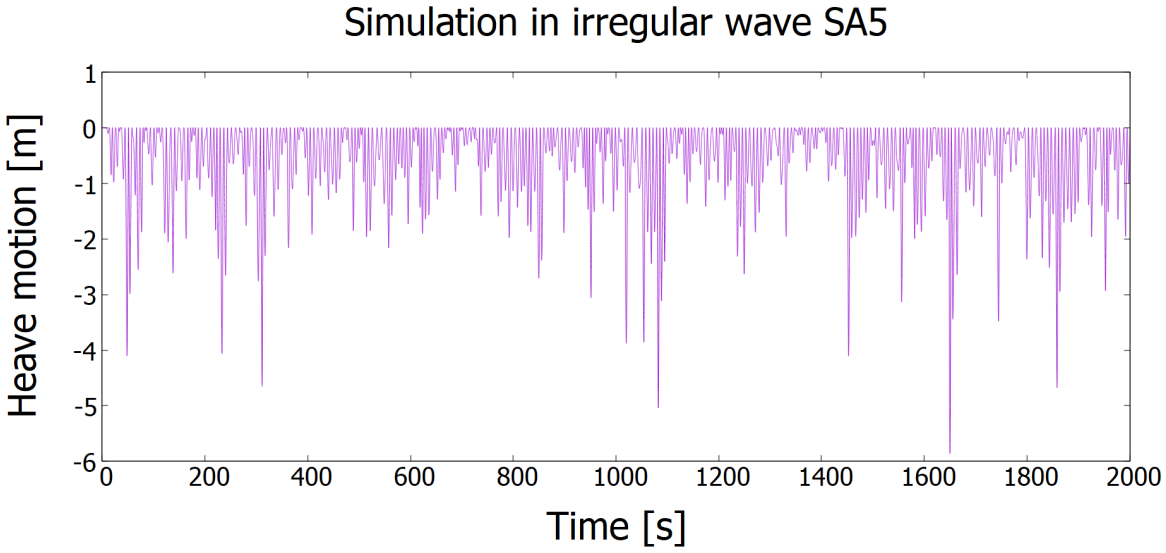


(a) Heave motion with irregular waves SA4

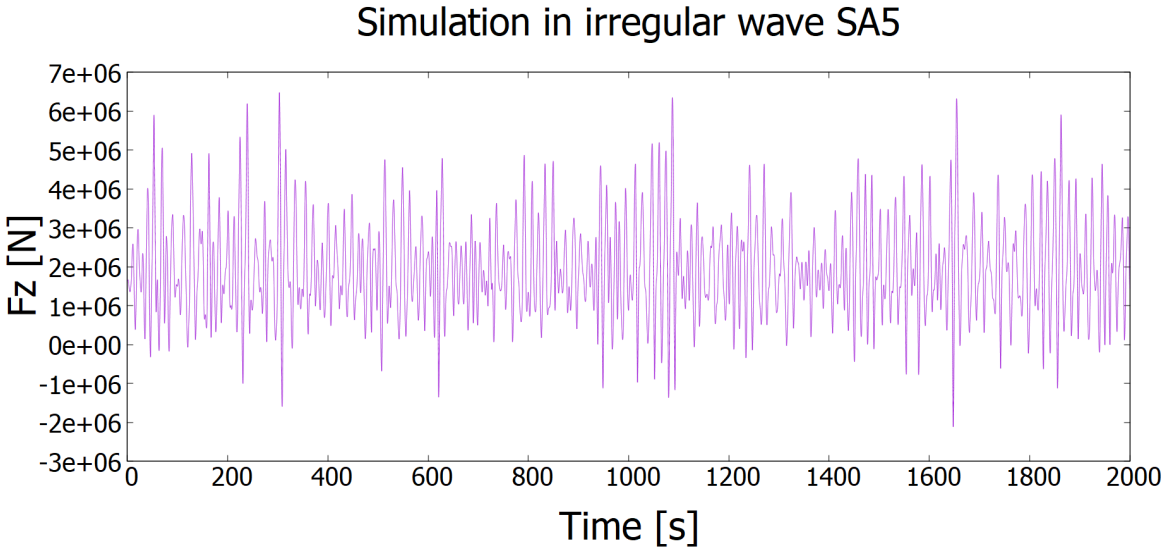


(b) z-component of the mooring forces with irregular waves SA5

Figure 7.23: Results of the simulations for heave motion and z-component of the mooring forces with irregular waves SA5

In the same way, for the sea state SA5 the minimum value in fig. 7.23 is -5.87 meters and the threshold of 90% of this value is exceeded once, while the threshold of 70% of this value is exceeded five times.

Concerning the forces on the moorings in the z direction they oscillates between a maximum and minimum value that are respectively $6.47 \cdot 10^6 N$ and -$2.11 \cdot 10^6 N$. The threshold of 90% of this maximum value is exceeded 4 times in this time history.

# Chapter 8

# Conclusions

This study explores the advancements in wave energy conversion through the numerical analysis of the C4 CorPower Wave Energy Converter within various wave scenarios. Initiated by outlining the pressing need for renewable energy sources, it then provides a thorough review of current WEC technologies, with a particular focus on the operational principles and classifications of these systems before presenting CorPower C4 characteristics. The thesis delves into the theoretical framework of wave-body interactions, employing linear potential-flow theory supplemented by corrections relating to nonlinear potential and viscous-flow effects to enhance the accuracy of its analyses.

Subsequently, the study goes into the numerical solution realm, using a frequency domain approach together with time domain simulations following Cummins' equation to model the dynamic responses of the WEC. Through a rigorous validation process with experimental data, the thesis confirms the reliability and accuracy of the employed software tools and modeling of the studied systems. Moreover through a numerical convergence study, it is highlighted the importance of nonlinear hydrodynamic effects and viscous effects for an accurate representation of WEC behavior under operational and harsh sea conditions.

Through a blend of theoretical insights and numerical analyses, the thesis successfully demonstrates the integration of linear potential-flow theory with viscous effects to accurately predict the WEC's dynamic response across various wave scenarios.

The thesis also presents additional enhancements to the linear theory that, while not integrated into the numerical solution for this study, offer potential avenues for future research. The limitations of the theory used in this study are due to the model's exclusion of highly nonlinear effects, which means it cannot explore phenomena like wave breaking or slamming, problem that can be simplified as described for example in [17]. These theoretical augmentations, left unexplored within the current work, present promising opportunities to further improve the accuracy and effectiveness of the modeling and the analysis of those systems. This statement opens the door to subsequent investigations aimed at realizing the full potential of these theoretical integrations. Concluding, future

studies should aim to model the actual WEC system rather than relying on the model used for experimental tests. This would include integrating the Power Take-Off and the relative heave motion between the buoy and its moorings.

# Acknowledgments

I would like to express my gratitude to my supervisor, Professor Giovanni Bracco; Engineer Andrea Bardazzi for his endless technical support; Professor Marilena Greco for her availability and patience in her guidance; and finally, Professor Claudio Lugni, for his support and inspiration.

I would also like to thank CorPower Ocean for their willingness to collaborate and the Norwegian University of Science and Technology (NTNU) in Trondheim, Norway, for hosting me during this project.

# Appendix A

# Python scripts

### A.0.1 Gmsh script for the meshed structure of the sphere

Listing A.1: Script for the structured sphere mesh

```
SetFactory("OpenCASCADE");
//+
Point(1) = {0.5, 0, 0, 1.0};
//+
Point(2) = {0, 0, 0.5, 1.0};
//+
Point(3) = {0, 0, 0, 1.0};
//+
Circle(1) = {1, 3, 2};
//+
//+

nth = 29;
nr  = nth - 1;


Extrude {{0, 0, 1}, {0, 0, 0}, Pi/2} {
  Curve{1}; Layers{nr}; Recombine;
}
Extrude {{0, 0, 1}, {0, 0, 0}, Pi/2} {
  Curve{4}; Layers{nr}; Recombine;
}
Extrude {{0, 0, 1}, {0, 0, 0}, Pi/2} {
  Curve{7}; Layers{nr}; Recombine;
```

```
}
Extrude {{0, 0, 1}, {0, 0, 0}, Pi/2} {
  Curve{10}; Layers{nr}; Recombine;
}
Transfinite Curve {1,4,7,10} = nth Using Progression -1;

Mesh 2;

Transfinite Surface {1} Right;
//+
//Transfinite Surface {1};
//+
//Recombine Surface {1};
//+

//+
Transfinite Curve {10} = 20 Using Progression 1;
//+
Curve{10} In Surface{3};
```

### A.0.2 Gmsh script for the meshed structure of the WEC hull

Listing A.2: Script for the WEC hull mesh

```
SetFactory("OpenCASCADE");

#define all the points of the profile of the hull

// Create a spline til point 17
Spline(1) = {1:16};

// Create a line
Line(2) = {16, 17};

// Line
Line(3) = {17, 18};

circ = 18;
nr   = circ - 1;
```

```
16
17 Extrude {{0, 0, 1}, {0, 0, 0}, Pi/2} {
18   Curve{1,2};Layers{nr}; Recombine;
19 }
20 Extrude {{0, 0, 1}, {0, 0, 0}, Pi/2} {
21   Curve{3};
22 }
23 Extrude {{0, 0, 1}, {0, 0, 0}, Pi/2} {
24   Curve{6,8};Layers{nr}; Recombine;
25 }
26 Extrude {{0, 0, 1}, {0, 0, 0}, Pi/2} {
27   Curve{10};
28 }
29 Extrude {{0, 0, 1}, {0, 0, 0}, Pi/2} {
30   Curve{13,15};Layers{nr}; Recombine;
31 }
32 Extrude {{0, 0, 1}, {0, 0, 0}, Pi/2} {
33   Curve{17};
34 }
35 Extrude {{0, 0, 1}, {0, 0, 0}, Pi/2} {
36   Curve{20,22};Layers{nr}; Recombine;
37 }
38 Extrude {{0, 0, 1}, {0, 0, 0}, Pi/2} {
39   Curve{24};
40 }
41
42 Transfinite Curve {1,6,13,20} = nr Using Progression -1;
43 Transfinite Curve {3,10,17,24,31} = 12 Using Progression -1;
```

### A.0.3 Script for the interpolated curve of the natural period function of the draft

Listing A.3: Script for the function of the natural period

```
1 import matplotlib.pyplot as plt
2 import numpy as np
3 from scipy.interpolate import interp1d
4
5 # Draft values and corresponding natural periods in seconds
```

```
drafts = np.array([0.49, 3.25, 5.47, 8.89, 12.4])  # meters
T_n = np.array([9.81, 4.88, 4.16, 9.97, 24.16])  # seconds

# Interpolating the data
f = interp1d(drafts, T_n, kind='cubic')

# Generating more points for a smoother curve
drafts_interp = np.linspace(min(drafts), max(drafts), num
    =1000)
T_n_interp = f(drafts_interp)

# Plotting
plt.figure(figsize=(8, 6))
plt.plot(drafts, T_n, 'o', label='Data points')
plt.plot(drafts_interp, T_n_interp, '-', label='Interpolated
    curve')
plt.xlabel('Draft (m)')
plt.ylabel('Natural Period (s)')
plt.title('Natural Period vs. Draft')
plt.legend()
plt.grid(True)
plt.show()
```

### A.0.4 Script for the interpolated curve of the added mass function of the draft

Listing A.4: Script for the function of the added mass

```
import matplotlib.pyplot as plt
import numpy as np
from sympy import symbols, prod, diff, lambdify

# Data
A_values = [144884, 118443, 87694, 50560, 5863]
#A_values = [144884/87694, 118443/87694, 87694/87694,
    50560/87694, 5863/87694] #to use for adimensional result
D_values = [12.4, 8.89, 5.47, 3.25, 0.49]
T_values = [1, 2, 3, 4, 5]

```

```
# Definition of D e T as symbols
D, T = symbols('D T')

# Calculation of Lagrange poly
lagrange_poly = sum(A * prod([(D - D_values[j]) / (D_values[i] - D_values[j]) for j in range(5) if j != i]) for i, A in enumerate(A_values))

# Calculation of the derivative of the function with respect to the draft
derivative_lagrange = diff(lagrange_poly, D)

# Calculation of dA/dD * dD/dT
result = derivative_lagrange * diff(sum(D * prod([(T - T_values[j]) / (T_values[i] - T_values[j]) for j in range(5) if j != i]) for i, D in enumerate(D_values)), T)

# Calculation of dA/dD * dD/dT as numerical funcion
result_func = lambdify(D, result, 'numpy')

# Array of values of D for the plot
D_values_plot = np.linspace(min(D_values), max(D_values), 1000)

# Array of interpolated values fot the Added mass
lagrange_func = lambdify(D, lagrange_poly, 'numpy')
A_values_plot = lagrange_func(D_values_plot)

# Calcularion of dA/dD * dD/dT with numerical method
result_values_plot = np.array([result_func(float(d)) for d in D_values_plot])

# Plot of Lagrange poly with respect to the original values
plt.figure(figsize=(8, 6))
plt.plot(D_values, A_values, 'ro', label='Original data')
plt.plot(D_values_plot, A_values_plot, label='Lagrange function')
plt.title('Variation of the heave added mass (A) with respect to the Draft (D)')
```

```
plt.xlabel('Draft (D)')
plt.ylabel('Heave added mass (A)')
plt.legend()
plt.show()
```

### A.0.5 Script for the interpolated curve of the diameter as function of the height of the structure

Listing A.5: Script for the function of the diameter

```
import numpy as np
import matplotlib.pyplot as plt

def diametro_altezza_completa(s):
    if  6.710 >= s >= -5.474:
        # WEC interpolato con un polinomio di grado 5: the
           coefficient are hidden for confidential issues
        return A1 * s**5 + A2 * s**4 + A3 * s**3 -\
            A4 * s**2 - A5 * s + A6

    elif  s > 6.710:
        # Higher part
        return 2.056
    elif -24.8 < s <= -5.474:
        # Tapered rod
        return 0.02
    elif -36.9 < s <= -24.8:
        # Rod housing
        return 0.068
    elif -46 < s <= -36.9:
        # Rod side
        return 0.024
    else:
        return 0

# Creazione di un intervallo di valori di s che copre sia la
   parte interpolata che quella a scalini
s_valori = np.linspace(12, -46, 1000)  # Copre l'intero
   intervallo da 0 a -46
```

```
27
28 # Calcolo dei valori di diametro per ogni valore di s
      utilizzando la funzione completa
29 x_valori = [diametro_altezza_completa(s) for s in s_valori]
30
31 # Plot del profilo completo della struttura
32 plt.figure(figsize=(8, 8))
33 plt.plot(x_valori, s_valori, label='Complete profile')
34 plt.xlabel('Diameter')
35 plt.ylabel('Height')
36 plt.title('Complete profile of the system')
37 plt.legend()
38 plt.grid(True)
39 plt.axis('equal')
40 plt.show()
```

# Bibliography


[1] EWEA (European Wind Energy Association) & Ocean Energy Europe. Ocean energy: Opportunities for global leadership. *EWEA and Ocean Energy Europe Joint Publication*, 2019.

[2] World energy outlook. *International Energy Agency*, 2023.

[3] Global energy review. *International Energy Agency*, 2020.

[4] J. Falnes. Ocean waves and oscillating systems: Linear interactions including wave-energy extraction. *Cambridge University Press*, 2002.

[5] Dongsheng Qiao, Rizwan Haider, Jun Yan, Dezhi Ning, and Binbin Li. Review of wave energy converter and design of mooring system. 2020.

[6] Yongxing Zhang, Yongjie Zhao, Wei Sun, and Jiaxuan Li. Ocean wave energy converters: Technical principle, device realization, and performance evaluation. *Renewable and Sustainable Energy Reviews*, 2021.

[7] CorPower Ocean. https://corpowerocean.com/.

[8] Faltinsen. Sea loads on ships and offshore structures. *Cambridge Ocean Technoogy Series*, 1990.

[9] W.E. Cummins. The impulse response function and ship motions. 1962.

[10] Giuseppe Giorgi. Nonlinear hydrodynamic modelling of wave energy converters under controlled conditions. 2018.

[11] M. Greco and C. Lugni. 3-d seakeeping analysis with water on deck and slamming. part 1: Numerical solver. *ScienceDirect*, 2012.

[12] Environmental conditions and environmental loads. *DNV-RP-C205*, 2014.

[13] Ling Wan, Marilena Greco, Claudio Lugni, Zhen Gao, and Torgeir Moan. A combined wind and wave energy-converter concept in survival mode: Numerical and experimental study in regular waves with a focus on water entry and exit. 2017.

[14] J.H. Mathews and K.K. Fink. Numerical methods using matlab 4 th edition. *Prentice-Hall Inc. New Jersey*, 2004.

[15] M. B. Kramer, J. Andersen, S. Thomas, F. B. Bendixen, H. Bingham, R. Read, N. Holk, E. Ransley, S. Brown, Yi-Hsiang Yu, T. T. Tran, J. Davidson, C. Horvath, C. Janson, K. Nelsen, and C. Eskilsson. Highly accurate experimental heave decay tests with a floating sphere: A public benchmark dataset for model validation of fluid–structure interaction. 2021.

[16] Gmsh: A three-dimensional finite element mesh generator with built-in pre and post-processing facilities. https://gmsh.info/.

[17] Faltinsen. Hydrodynamics of high-speed marine vehicles. *Cambridge University Press*, 2006.